KU LEUVEN

FACULTEIT INGENIEURSWETENSCHAPPEN

Exploiting Sparsity for Registration of Brain Tumor MR Images

Xavier Garcia Pich

Thesis submitted for the degree of
Telecommunications Engineering

Thesis supervisor:
prof. dr. ir. Frederik Maes

Mentors:
dr. Thijs Dhollander
ir. Tom Haeck

Academic year 2013 – 2014

Preface

I would like to express my gratitude to UPC and KUL for granting me the opportunity for writing this thesis abroad, and to my parents Josep and Mercè to make it happen. I would like to thank Thijs and Tom for their tips, dedication and patience shown day by day. Specially thanks to Roger for accompanying me through this path not always pleasant; thanks for being a wonderwall. You have a friend here. Finally, I would like to thank all the inspiring people I've met during this Erasmus. Thanks to you all.

Xavier Garcia Pich

Contents

Preface i

Abstract iii

List of Figures and Tables iv

List of Abbreviations and Symbols vii

1 Background 1
- 1.1 Sparsity . . . 1
- 1.2 Image Registration . . . 4
- 1.3 Thesis Layout . . . 5

2 Problem Statement 7

3 Methods 9
- 3.1 Dissimilarity Measures . . . 10
- 3.2 Regularizers . . . 15
- 3.3 Transformation Models . . . 16
- 3.4 Optimization Strategy . . . 20
- 3.5 Validation . . . 20

4 Materials 23
- 4.1 Data . . . 23
- 4.2 Ground Truth . . . 24

5 Experiments 29
- 5.1 Experiment 1: Parameter Tuning . . . 29
- 5.2 Experiment 2: Tumor Mass Effect . . . 31
- 5.3 Experiment 3: Tumor Infiltration . . . 37

6 Discussion and Future Work 43
- 6.1 Future Work . . . 44

7 Conclusions 47

Bibliography 49

Abstract

In medical imaging, sparsity has been used in the acquisition and reconstruction of MRI images, image denoising and face recognition among others. The aim of this thesis is to assess whether exploiting sparsity is a desirable property in the problem of brain tumor image registration. To this end, we consider tumor mass effect and tumor infiltration as two different tumor growing effects.

In intensity-based nonrigid image registration, an optimization problem is defined by the minimization of a cost function with respect to the transformation parameters. This cost function consists of a dissimilarity term between the images being registered and a term that regularizes the transformation. Within this thesis, a modified ℓ_1 norm dissimilarity measure and a modified ℓ_1 regularization term are constructed. We compare the performance of different algorithms that combine these contributions with an ℓ_2 norm dissimilarity measure and diffusion regularizer for three different transformation models. Methods are tested on simulated brain tumor MR images and the validation of the registration is done by computing two dissimilarity distances between the deformation field obtained and a simulated ground truth.

Results show that algorithms that use the modified ℓ_1 regularizer and a ℓ_2 dissimilarity measure recover the deformation of the tumor, while algorithms that use the modified ℓ_1 norm dissimilarity measure in some situations do not.

List of Figures and Tables

List of Figures

1.1 Solution to (1.7) in the 2D case. 3
1.2 Solution to (1.8) in the 2D case. 3

3.1 Image Registration Process 10
3.2 Solution to (1.8) in the 2D case and plot of the unit ℓ_2 circle. 12
3.3 Solution to (1.7) in the 2D case and plot of the unit ℓ_1 circle. 13
3.4 Solution to (3.13) in the 2D case and plot of the unit modified ℓ_1 circle for $\epsilon = 1e^{-3}$ 13
3.5 Solutions to (1.7), (1.8) and (3.13) in the 2D case and plot of the unit ℓ_p circles for $p = 1, 2$ and $\epsilon = \{1e^{-3}, 1e^{-2}, 1.5e^{-1}, 1\}$. 14

4.1 Skull stripping: intermediate images. In the first row: the original image (left), the filtered image (middle) and the edge image mask (right). In the second row: the isolated brain mask (left), the brain mask after applying morphological erosion (middle) and the extracted brain image (right). . 24
4.2 Generation of a local expansion in a deformation field. 25
4.3 Ground truth generation process for mass effect 26
4.4 Intermediate images in the mass effect ground truth generation process From left to right: the floating image with the pathology (left), the ground truth deformation field generated (middle) and the reference image with the tumor mass effect (right). The yellow square in the first image indicates the location in which the second image is zoomed. . . . 26
4.5 Ground truth generation process for tumor infiltration 27
4.6 Intermediate images in the infiltration ground truth generation process From left to right: the floating image with the pathology (left), the ground truth deformation field generated (middle) and the reference image with the tumor infiltration (right). 28

5.1 Tumor mass effect data set input images. From left to right: floating image, reference image, ground truth deformation field and deformation field after registration. Subjects 04, 06, 20, 38 and 52 are displayed from top to bottom. 32

5.2 In columns, the initial overlap image and the final overlap image. In rows, visual assessment of $\mathcal{A}^{\text{param}}_{\ell_2,\ \text{diff}}$, $\mathcal{A}^{\text{param}}_{\ell_2,\ \text{mod}-\ell_1}$ and $\mathcal{A}^{\text{non param}}_{\ell_2,\ \text{diff}}$ registration algorithms. 33
5.3 Rows 1 and 2: intensity difference image. Rows 3 and 4: deformation fields. First image in rows 1 and 3 shows the initial floating image case. Then, algorithms $\mathcal{A}^{\text{param}}_{\ell_2,\ \text{diff}}$, $\mathcal{A}^{\text{param}}_{\ell_2,\ \text{mod}-\ell_1}$ and $\mathcal{A}^{\text{non param}}_{\ell_2,\ \text{diff}}$ are displayed in order. 34
5.4 Visual assessment of $\mathcal{A}^{\text{param}}_{\text{mod}-\ell_1,\ \text{diff}}$ and $\mathcal{A}^{\text{non param}}_{\text{mod}-\ell_1,\ \text{diff}}$ algorithms. In columns, the overlap image before registration, the final overlap image using $\mathcal{A}^{\text{param}}_{\text{mod}-\ell_1,\ \text{diff}}$ algorithm, and the final overlap image using $\mathcal{A}^{\text{non param}}_{\text{mod}-\ell_1,\ \text{diff}}$ algorithm. 35
5.5 Visual assessment of $\mathcal{A}^{\text{param}}_{\text{mod}-\ell_1,\ \text{diff}}$ and $\mathcal{A}^{\text{non param}}_{\text{mod}-\ell_1,\ \text{diff}}$ registration algorithms. First row shows the intensity difference image before (column 1) and after registration (columns 2 and 3). Second row shows the ground truth deformation field (column 1) and the deformation field after registration (columns 2 and 3. 36
5.6 Tumor infiltration data set input images. In columns, floating image, reference image, ground truth deformation field and deformation field after registration. Subjects 04, 06, 20, 38 and 52 are displayed from top to bottom. 38
5.7 In columns, the initial overlap image, and the final overlap images. In rows, visual assessment of $\mathcal{A}^{\text{non param}}_{\ell_2,\ \text{diff}}$, $\mathcal{A}^{\text{non param}}_{\ell_2,\ \text{mod}-\ell_1}$ and $\mathcal{A}^{\text{param}}_{\ell_2,\ \text{diff}}$. 39
5.8 Visual assessment of $\mathcal{A}^{\text{param}}_{\ell_2,\ \text{diff}}$, $\mathcal{A}^{\text{param}}_{\ell_2,\ \text{mod}-\ell_1}$ and $\mathcal{A}^{\text{non param}}_{\ell_2,\ \text{diff}}$ registration algorithms. First row shows the intensity difference image before (column 1) and after registration (columns 2, 3 and 4). Second row shows the ground truth deformation field (column 1) and the deformation field after registration (columns 2, 3 and 4). 40
5.9 Visual assessment of $\mathcal{A}^{\text{param}}_{\text{mod}-\ell_1,\ \text{diff}}$ and $\mathcal{A}^{\text{non param}}_{\text{mod}-\ell_1,\ \text{diff}}$ algorithms. In columns, the overlap image before registration, the final overlap image using $\mathcal{A}^{\text{param}}_{\text{mod}-\ell_1,\ \text{diff}}$ algorithm, and the final overlap image using $\mathcal{A}^{\text{non param}}_{\text{mod}-\ell_1,\ \text{diff}}$ algorithm. 40
5.10 Visual assessment of $\mathcal{A}^{\text{param}}_{\text{mod}-\ell_1,\ \text{diff}}$ and $\mathcal{A}^{\text{non param}}_{\text{mod}-\ell_1,\ \text{diff}}$ registration algorithms. First row shows the intensity difference image before (column 1) and after registration (columns 2 and 3). Second row shows the ground truth deformation field (column 1) and the deformation field after registration (columns 2 and 3). 41

List of Tables

3.1 Solutions to Eq. (1.7), (1.8) and (3.12) for the 2D case. 14

5.1 Parameter selection for the algorithms tested in the tumor mass effect subjects. 30

5.2 Parameter selection for the algorithms tested in the tumor infiltration subjects. 30
5.3 Registration evaluations of the tumor mass effect data set. The first row in each algorithm is for the global d_{SSD} distance and the second row is for the local d_{J} distance. 31
5.4 Registration evaluations of the tumor infiltration data set. The first row in each algorithm is for the global d_{SSD} distance and the second row is for the local d_{J} distance. 37

List of Abbreviations and Symbols

Abbreviations

MR	magnetic resonance
BC	brightness constraint
SSD	sum of squared differences
$affine$	affine transformation model
$non\ param$	non parametric dense deformation field transformation model
$param$	parametric dense deformation field transformation model

Symbols

Vectors, Matrices and Images

$\mathbb{R}^n$	space of real-valued n-vectors
$\mathbb{R}^{m\times n}$	space of real-valued $(m \times n)$ matrices
$\mathbb{R}^+$	space of positive real-valued numbers
$\mathbb{C}^n$	space of complex-valued n-vectors
$\mathbb{C}^{m\times n}$	space of complex-valued $(m \times n)$ matrices
$\mathbb{N}$	space of natural-valued numbers
$\mathbf{x}$ (lower case, bold)	vector in $\mathbb{R}^n$
x_j	j^{th} component of $\mathbf{x}$
$\mathbf{X}$ (upper case, bold)	matrices in $\mathbb{R}^{m\times n}$
$\|\mathbf{x}\|_p$	vector ℓ_p norm
R or $R(\mathbf{x})$	scalar-valued reference image (evaluated at $\mathbf{x}$)
F or $F(\mathbf{x})$	scalar-valued floating image (evaluated at $\mathbf{x}$)

Deformations

$\mathbf{u}$ or $\mathbf{u}(\mathbf{x})$	vector-valued deformation field (evaluated at $\mathbf{x}$)
$F^{\mathbf{u}}$ or $F^{\mathbf{u}}(\mathbf{x})$	floating image warped according to displacement $\mathbf{u}$ (evaluated at $\mathbf{x}$)

Functionals

E	energy term
$\mathcal{S}(R, F^{\mathbf{u}})$	dissimilarity measure
$\mathcal{R}(\mathbf{u})$	regularizer
r	residual image
Ψ_r	penalty function

Parameters

λ	regularization parameter
ϵ	sparsity parameter
τ	step size
w	weight of the Gaussian distribution
σ	standard deviation of the Gaussian distribution

Chapter 1

Background

This thesis incorporates two main concepts. The first one is sparsity, a mathematical property and a tool used in medical imaging. Both concepts will be introduced in this first chapter.

1.1 Sparsity

The term sparsity refers to a measurable property of a vector or matrix. The sparsity of a vector is defined by the number of non zero entries of that vector:

$$\|\mathbf{x}\|_0 = \#\{k : \ x_k \neq 0, k = 1, ..., n\} \tag{1.1}$$

For example, the sparsity of a vector $\mathbf{x_1} = (0, 1, 0, 0)^T$ is 1 and the sparsity of a vector $\mathbf{x_2} = (0, 1, 0.04, 0.001)^T$ is 3. In the previous example, $\mathbf{x_1}$ is a 1-sparse vector while $\mathbf{x_2}$ is a 3-sparse vector; $\mathbf{x_1}$ is sparser than $\mathbf{x_2}$.

Sparsity is used in compressed sensing for the recovery of signals from highly incomplete data[1, 2, 3]. Results from these papers declare that a sparse vector $\mathbf{x} \in \mathbb{R}^n$ can be recovered from a small number of linear measurements $\mathbf{b} = \mathbf{A}\mathbf{x} \in \mathbb{R}^k, \ k \ll n$ by solving a convex program. This procedure is implemented in [4] for seven different contexts. In medical imaging, sparsity has been incorporated in the acquisition and reconstruction of MRI images [5], image denoising by wavelet thresholding [6, 7] and face recognition [8] among other applications.

Furthermore, working with sparse vectors and matrices is in most cases beneficial because it requires less storage memory and computations between them can be done more efficiently since we only need the values and positions of the non zero entries of the vectors/matrices.

Sparse Representation and Approximations

Suppose we are given a vector $\mathbf{b} \in \mathbb{C}^m$ and a matrix $\mathbf{A} \in \mathbb{C}^{m \times n}$, we want to find a vector $\mathbf{x} \in \mathbb{C}^n$ such that:

$$\mathbf{A}\mathbf{x} = \mathbf{b}. \tag{1.2}$$

In general, the matrix $\mathbf{A}$ is overcomplete, i.e., there are less rows than columns ($m \ll n$)[9]. Therefore, the above problem does not have a unique solution. Since there exists a choice of solution, a sparse vector might be desirable depending on the problem at hand.

The above problem is relaxed by not requiring the vector $\mathbf{x}$ to reproduce $\mathbf{b}$ exactly. Suppose again the vector $\mathbf{b} \in \mathbb{C}^m$, the matrix $\mathbf{A} \in \mathbb{C}^{m \times n}$ and a tolerance $\epsilon \in \mathbb{R}^+$, we want to find a vector $\mathbf{x} \in \mathbb{C}^n$ such that:

$$\|\mathbf{A}\mathbf{x} - \mathbf{b}\| < \epsilon. \tag{1.3}$$

If a sparse vector $\mathbf{x}$ is found, it is not called a sparse representation of $\mathbf{b}$ but a sparse approximation. Therefore, a representation is sparse when a large number of components have a very small contribution to the image (or even no contribution at all).

Computing a Sparse Solution

In this work, we will be using the ℓ_p norms. The general definition of the ℓ_p norm of a vector is:

$$\|\mathbf{x}\|_p := \left(\sum_{i=1}^{n} |x_i|^p \right)^{1/p}, \ p \in \mathbb{N} \tag{1.4}$$

Suppose we are given the constraint $\mathbf{A}\mathbf{x} = \mathbf{b}$ and we want to find the smallest vector that satisfies this restriction. We can formulate this as:

$$\min_{\mathbf{x}} \quad \|\mathbf{x}\|_p \quad s.t. \ \mathbf{A}\mathbf{x} = \mathbf{b} \tag{1.5}$$

In general, we can approach this problem using different ℓ_p norms. But since we are interested in finding a sparse vector $\mathbf{x}$ we will use the ℓ_0 norm, as explained in the previous section. Then, the problem (1.5) can be written as the sparse problem:

$$\min_{\mathbf{x}} \quad \|\mathbf{x}\|_0 \quad s.t. \ \mathbf{A}\mathbf{x} = \mathbf{b} \tag{1.6}$$

This problem is a NP-hard problem and it can be relaxed by using the ℓ_1 norm instead. This strategy is called Basis Pursuit [10]. The general problem (1.5) can be rewritten as:

$$\min_{\mathbf{x}} \quad \|\mathbf{x}\|_1 \quad s.t. \ \mathbf{A}\mathbf{x} = \mathbf{b} \tag{1.7}$$

$$\text{2D case:} \quad \min_{\mathbf{x}} \quad |x_1| + |x_2| \quad s.t. \ \mathbf{A}\mathbf{x} = \mathbf{b}$$

For the 2D case, this problem is visualized in Figure 1.1. It shows the solution to this problem where one of the components of the vector $\mathbf{x}$ found is zero. Hence, the solution found is sparse.

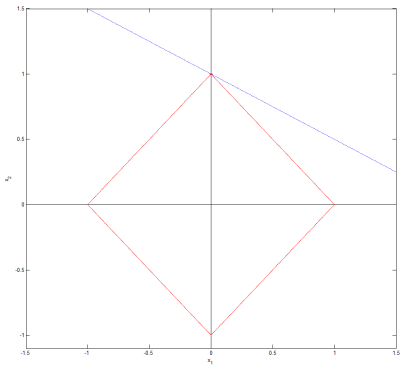

Figure 1.1: Solution to (1.7) in the 2D case.

Conversely, using the ℓ_2 norm for the general problem (1.5) does not generate a sparse solution. For this case, Eq. (1.5) can be rewritten as:

$$\min_{\mathbf{x}} \quad \|\mathbf{x}\|_2 \quad s.t.\ \mathbf{Ax} = \mathbf{b} \tag{1.8}$$

$$\text{2D case:} \quad \min_{\mathbf{x}} \quad \sqrt{x_1^2 + x_2.^2} \quad s.t.\ \mathbf{Ax} = \mathbf{b}$$

Figure 1.2 illustrates the solution to Eq. (1.8). Here, none of the components of the solution is equal to zero. Hence, using the ℓ_1 norm in the problem (1.5) generates a sparser solution than using the ℓ_2 norm.

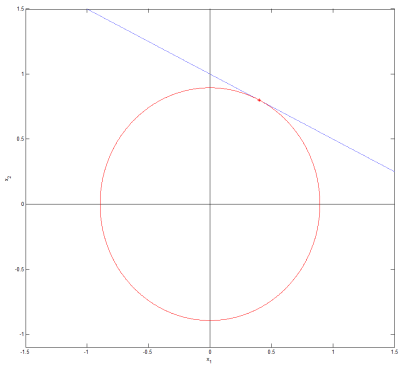

Figure 1.2: Solution to (1.8) in the 2D case.

1.2 Image Registration

Over the last few decades, image registration has become a key component for a large number of clinical applications such us intervention and treatment planning, monitoring of diseases, computer-aided diagnosis or radiation therapy.

In image registration, one image (floating image) is spatially mapped onto another image (reference image) such that anatomically equivalent structures in both images are aligned. This spatial alignment is required to properly integrate useful information from the separate images.

The first registration techniques performed registration by adjusting rotations and translations manually. This was done by translating the contours of one image onto a second one. Huge drawbacks of this manual procedure are the lack of reproducibility and observer errors that result from external conditions, experience or possible mistakes [11]. Therefore, through the years automatic registration algorithms are becoming increasingly important. Here, rotations and translations are not adjusted manually. An important group of image registration is variational registration where a cost function is minimized with respect to the desired transformation parameters. Thus, registration algorithms can be cataloged according to the space to which the transformation belongs. Rigid or affine registration algorithms depend on a few parameters, but in general are very limited and not descriptive enough to capture subtle anatomical differences between subjects. For these situations, nonrigid registration allow anatomical structures to be spatially mapped between images in a non rigid way[12, 13].

The cost function to minimize in variational image registration usually has two terms. The first one is an energy term that penalizes the dissimilarity of the images being registered. The second term in the cost function is called a regularization term. In general, image registration is ill-posed. Adding a regularization term to the cost function penalizes unwanted transformations. The choice of a certain dissimilarity measure or regularization term is application dependent and usually the right choice is not known beforehand.

Within the context of medical image registration, we consider the registration of brain tumor MR images of a subject in order to provide additional information for a more accurate diagnosis for the patient's treatment. Tumor growing behaviors can be explained by two main effects: a mass effect and an infiltration. A mass effect or volume expansion of the tumor means that the tumor spreads beyond the primary tissue into surrounding healthy tissues. On the other hand, in an infiltration expansion, healthy tissue is replaced by the expanded tumor tissue but the healthy tissue remains in its place.

1.3 Thesis Layout

The organization of this thesis is detailed as follows:

- Chapter 2 states the problem we are trying to solve in this thesis. We clarify the motivation of this work and we give some insights into how we are going to solve it.
- Chapter 3 discusses the methodology of the study. The dissimilarity measures, regularization terms and transformation models are formulated. Furthermore, the regularization strategy and the validation methods are described.
- Chapter 4 describes the data used in the experiments and explains how we generate the ground truth for later validation.
- Chapter 5 describes all the experiments and presents the validation results.
- Chapter 6 gives a discussion of the results. We also point out perspectives for further research and improvements to be made.

Chapter 2

Problem Statement

By incorporating sparsity in the registration problem, we believe we can improve the registration of brain MR images in case there is a tumor present.

Suppose we have a pair of images with a tumor present of the same patient at two different time points. We want to register both images in order to provide additional information for future treatment of the patient. Consider the intensity difference image between them after being registered. Since a good registration algorithm would recover the tumor deformation, this image would consist all zeros except for misregistration errors. That makes us believe that this image is a sparse representation, since most of its components have a small (or even null) contribution to the image. Similarly, a sparse deformation field would only have a deformation in the tumor location and not throughout the grid.

There may be different ways to enforce sparsity onto the registration problem but we focused in two in particular. First, we enforce sparsity in the dissimilarity measure term in the cost function of the registration problem by using a modified version of the ℓ_1 norm of the images to be registered. We assume the intensity difference images between them is small. A second option of enforcing sparsity in the registration problem is in the regularization term of the registration problem. In this case, we use what we call the modified ℓ_1 regularizer which imposes sparsity on the gradient of a deformation field. In this case, we want large deformations in the deformation field to be local and not global through the whole grid.

To assess whether sparsity is useful in our application, methods are tested on simulated brain tumor MR images and then evaluated through the comparison of two distances of the deformation field obtained with a simulated ground truth.

Chapter 3

Methods

The goal of image registration is to estimate a mapping between a pair of images. One image is assumed to remain stationary (the reference or target image), where the other (the floating or moving image) is spatially transformed to anatomically match it. In order to transform the floating image to anatomically match the reference image, a mapping is defined over the whole image. This mapping can be thought of as a function of a set of estimated transformation parameters.

Consider R the reference image and F the floating image, both as functions in $\mathbb{R}^n$. In the deformation $\Phi : \mathbb{R}^n \to \mathbb{R}^n$:

$$\Phi(\mathbf{x}) = \mathbf{x} - \mathbf{u}(\mathbf{x}), \tag{3.1}$$

$\mathbf{u}$ is the displacement. Then, registration aims to find the displacement that minimizes a dissimilarity term $\mathcal{S}$ which measures the dissimilarity between the reference image R and the deformed floating image $F^{\mathbf{u}} := F(\Phi)$.

$$\min_{\mathbf{u}} \quad \mathcal{S}(R, F^{\mathbf{u}}). \tag{3.2}$$

To ensure that the minimization problem is well-posed and has a smooth solution, a regularization term $\mathcal{R}$ must be added to the dissimilarity term. Combining both the similarity and the regularization terms enables us to state the general form of the registration problem:

$$\min_{\mathbf{u}} \quad E(R, F^{\mathbf{u}}) = \min_{\mathbf{u}} \quad \mathcal{S}(R, F^{\mathbf{u}}) + \lambda \mathcal{R}(\mathbf{u}), \tag{3.3}$$

where λ is the trade-off between the dissimilarity measure and the regularizer. We are interested in methods for finding the deformation field $\mathbf{u}$ that minimizes Eq. (3.3).

Figure 3.1 illustrates the different components that define the registration problem[14]. An optimization of the transformation parameters is done through a minimization of the cost function $E(R, F^{\mathbf{u}})$. The transformation parameters are first initialized. At each iteration, the floating image is resampled according to the new parameter set. In the optimization process we consider a transformation model

representing the prior knowledge on the transformation to be found and the energy model to minimize. The energy model consists of a dissimilarity term between the reference image and the transformed floating image and a regularization term for the deformation field.

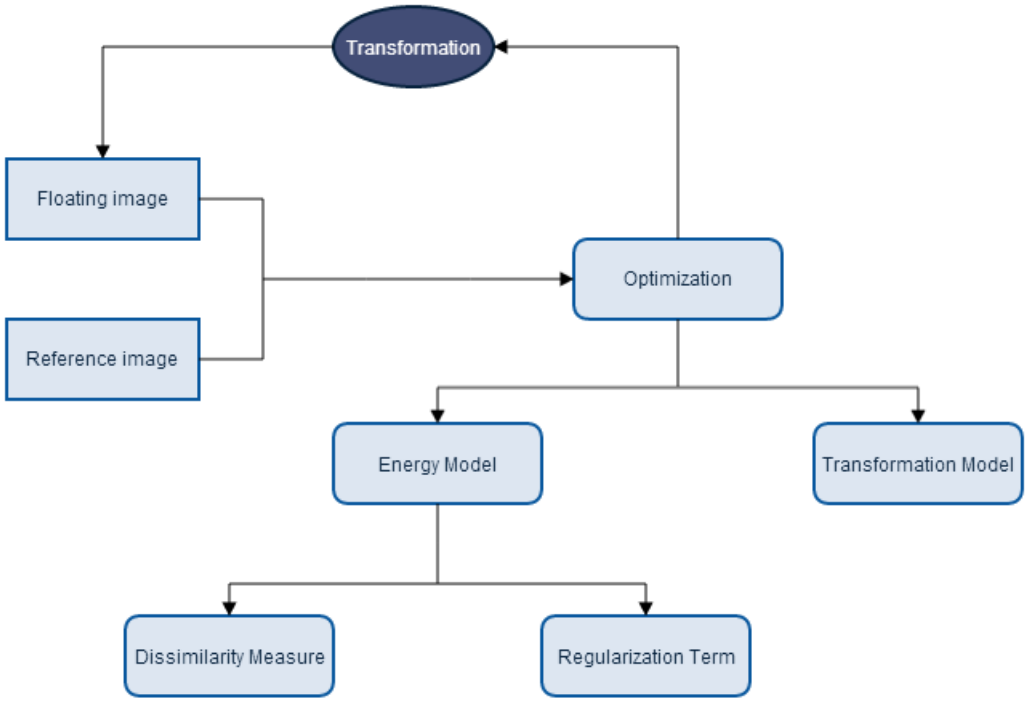

Figure 3.1: Image Registration Process

3.1 Dissimilarity Measures

Any dissimilarity measure relies on some assumption about the relationship between the images being registered. In medical image registration, constancy assumptions are useful when the floating and the reference images are of the same patient and from the same modality [12]. The simplest assumption that can be made about this relationship for the targeted application is that brightness is preserved between the images being registered.

$$F^{\mathbf{u}(\mathbf{x})} = R(\mathbf{x}) \quad \forall \mathbf{x} \in \Omega \tag{3.4}$$

This is called the brightness constancy constraint (BC), and it is applicable when images are captured from the same sensor under the same conditions.

Assuming the brightness constancy constraint for the images being registered, any misalignment between them should cause a deviation from this assumed constraint. Then, image dissimilarity measures can be constructed in order to penalize this deviation[12]. We begin by defining an image of residuals r that quantifies the deviation of two images from the assumed constancy constraint. For the brightness constancy constraint, this image is given by:

$$r_{BC}(\mathbf{x}; R, F^{\mathbf{u}}) = F^{\mathbf{u}}(\mathbf{x}) - R(\mathbf{x}). \tag{3.5}$$

Global image dissimilarity measures can be constructed applying a non negative function Ψ to the residual image r:

$$\mathcal{S}_{\Psi,r}(R, F^{\mathbf{u}}) = \int \Psi(r(\mathbf{x}; R, F^{\mathbf{u}}))\ d\mathbf{x} \tag{3.6}$$

Several choices can be made for the penalty function $\Psi(r(\mathbf{x}; R, F^{\mathbf{u}}))$. Among the most common penalty functions and for the purpose of this thesis, the penalty function $\Psi(r(\mathbf{x}; R, F^{\mathbf{u}}))$ is chosen such that:

$$\Psi_p(r) = |r|^p, \qquad p \in \mathbb{N} \tag{3.7}$$

The $|\cdot|^p$ function turns (3.7) into a penalty function of ℓ_p norm of the scalar valued residual image.

In this work, as explained in Chapter 1, we compare the performance during registration with the ℓ_2 norm, more commonly known as sum of squared differences, with the ℓ_1 norm or sum of absolute differences. For these cases, we can rewrite Eq. (3.6) as:

$$\mathcal{S}_{\ell_2}(R, F^{\mathbf{u}}) = \int (F^{\mathbf{u}}(\mathbf{x}) - R(\mathbf{x}))^2\ d\mathbf{x} \tag{3.8}$$

$$\mathcal{S}_{\ell_1}(R, F^{\mathbf{u}}) = \int |F^{\mathbf{u}}(\mathbf{x}) - R(\mathbf{x})|\ d\mathbf{x}\ , \tag{3.9}$$

where $\mathcal{S}_{\ell_2} = \mathcal{S}_{\Psi_2}$ and $\mathcal{S}_{\ell_1} = \mathcal{S}_{\Psi_1}$.

The main issue with the ℓ_1 norm in Eq. (3.9) is that it is not differentiable at zero. This problem is present when computing the derivative of this dissimilarity measure to the parameter set in the search of the best transformation parameters in the optimization problem. To tackle this problem inherent with ℓ_1 minimization, a modified version of $\mathcal{S}_{\Psi_1}$ is proposed in [12], called the modified ℓ_1 norm. This penalty function can be defined as:

$$\Psi_{1,\epsilon}(r) = \sqrt{r^2 + \epsilon}\ \ ,\ \epsilon \in \mathbb{R}^+ \tag{3.10}$$

which for small ϵ behaves like Ψ_1 but is differentiable everywhere. In this thesis, we call ϵ the sparsity parameter. With this new penalty function, the dissimilarity measure in Eq. (3.9) can be rewritten for the modified ℓ_1 norm case:

$$\mathcal{S}_{\text{mod}-\ell_1}(R, F^{\mathbf{u}}) = \int \sqrt{(F^{\mathbf{u}}(\mathbf{x}) - R(\mathbf{x}))^2 + \epsilon}\ d\mathbf{x}\ , \tag{3.11}$$

where $\mathcal{S}_{\text{mod}-\ell_1} = \mathcal{S}_{\Psi_{1,\epsilon}}$.

3.1.1 Modified ℓ_1 norm

In the previous section, we described the dissimilarity measures that will be used in this thesis. In Chapter 1, we explained how the ℓ_0 norm and the ℓ_1 norm find sparse solutions. However, we haven't seen whether the modified ℓ_1 norm version also finds sparse solutions or not. It is also useful to know how good this modified ℓ_1 norm can approximate the real ℓ_1 norm, depending on the sparsity parameter ϵ.

We sum up the general problem we introduced in the first section in Chapter 1 for reference:

$$\min_{\mathbf{x}} \quad \|\mathbf{x}\|_p \quad s.t. \quad \mathbf{Ax} = \mathbf{b}. \tag{3.12}$$

We explained how the use of the ℓ_0 norm finds a sparse solution but it turns (3.12) into a NP-hard problem. Furthermore, we saw how the ℓ_1 norm also find a sparse solution but the ℓ_2 did not. Figure 3.2 and Figure 3.3 illustrate this behavior.

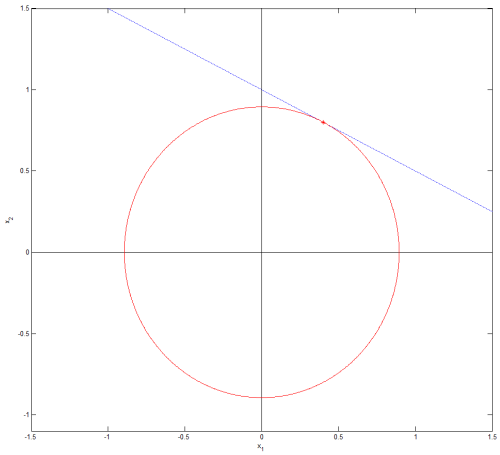

Figure 3.2: Solution to (1.8) in the 2D case and plot of the unit ℓ_2 circle.

It is useful to check whether the introduced modified ℓ_1 norm finds sparse solutions or not. Using the modified ℓ_1 norm, we can rewrite Eq. (3.12) as:

$$\min_{\mathbf{x}} \quad \sqrt{x_1^2 + \epsilon} + \sqrt{x_2^2 + \epsilon} \quad s.t. \quad \mathbf{Ax} = \mathbf{b}, \tag{3.13}$$

for $\epsilon \in \mathbb{R}^+$. Here, different solutions can be found depending on the value of the sparsity parameter ϵ. Figure 3.4 shows the behavior of the Eq. (3.13) for a given ϵ. If ϵ is small enough, it behaves like the ℓ_1 norm.

In Figure 5.4, for smaller ϵ the solution $\mathbf{x}$ found using the modified ℓ_1 norm tends

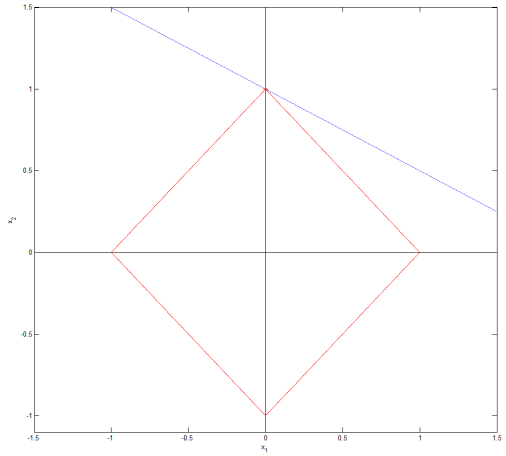

Figure 3.3: Solution to (1.7) in the 2D case and plot of the unit ℓ_1 circle.

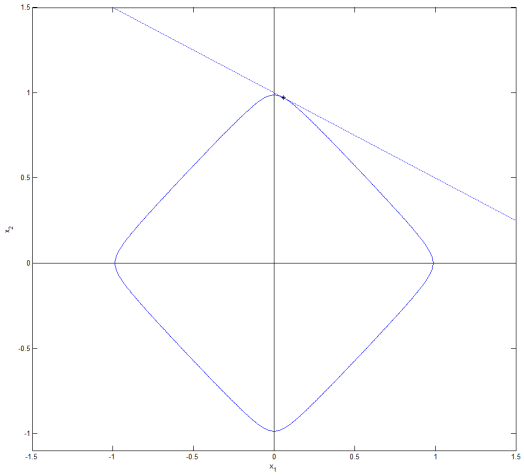

Figure 3.4: Solution to (3.13) in the 2D case and plot of the unit modified ℓ_1 circle for $\epsilon = 1e^{-3}$

to the one found using the ℓ_1 norm (Eq. (1.7) in Chapter 1). However, if ϵ increases, the solution tends to the one found using the ℓ_2 norm (Eq. (1.8) in Chapter 1). Figure 3.5 shows these behaviors for different ϵ values in the 2D case. The red plots are the ℓ_1 and ℓ_2 norms (Eq. (1.7) and (1.8) respectively), while the blue plots are the modified ℓ_1 norms (Eq. (3.13)).

In addition to that, Table 3.1 lists components x_1 and x_2 for the Eq. (1.7), (1.8) and (3.13) plotted in Figure 3.5. As said, depending on the sparsity parameter ϵ, one can get a sparse approximation to the minimization problem in (3.12).

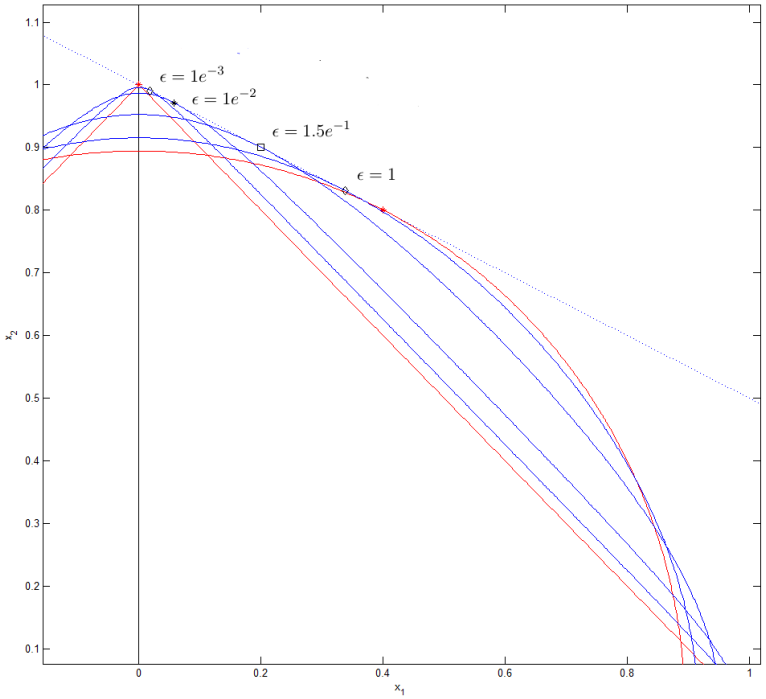

Figure 3.5: Solutions to (1.7), (1.8) and (3.13) in the 2D case and plot of the unit ℓ_p circles for $p = 1, 2$ and $\epsilon = \{1e^{-3}, 1e^{-2}, 1.5e^{-1}, 1\}$.

$\ell_\mathbf{p}$ **norm metric**	**epsilon**	$\mathbf{x_1}$	$\mathbf{x_2}$	$\mathbf{f(x)}$
$\ell_\mathbf{2}$ **norm**	-	0.3996	0.8002	0.8944
$\ell_\mathbf{1}$ **norm**	-	0	1	1
Modified $\ell_\mathbf{1}$ **norm**	$1.0e^{-3}$	0.0183	0.9909	1.0279
Modified $\ell_\mathbf{1}$ **norm**	$1.0e^{-2}$	0.0573	0.9714	1.0917
Modified $\ell_\mathbf{1}$ **norm**	$1.5e^{-1}$	0.2000	0.9000	1.1416
Modified $\ell_\mathbf{1}$ **norm**	1.0	0.3374	0.8313	2.3558

Table 3.1: Solutions to Eq. (1.7), (1.8) and (3.12) for the 2D case.

Derivatives of the Dissimilarity Measures

By minimizing a cost function with respect to the transformation parameters, the proper anatomical mapping between the reference image and the transformed floating image can be found. Without considering the regularization term, the registration problem can be written as:

$$\min_{\mathbf{u}} \quad E(R, F^{\mathbf{u}}) = \min_{\mathbf{u}} \quad \mathcal{S}(R, F^{\mathbf{u}}). \tag{3.14}$$

In order to find the deformation field, it is necessary to determine the variational derivative of the dissimilarity measure with respect to variations in the displacement field. For a general dissimilarity measure $\mathcal{S}(R, F^{\mathbf{u}})$, the variational derivative is defined in the direction $\mathbf{w}$ by:

$$d\mathcal{S}(R, F^{\mathbf{u}}; \mathbf{w}) = \lim_{h \to 0} \frac{1}{h} \left[\mathcal{S}\left(R, F^{\mathbf{u}+h\mathbf{w}}\right) - \mathcal{S}(R, F^{\mathbf{u}}) \right] \tag{3.15}$$

For any constancy assumption, the derivation of the general dissimilarity measure $\mathcal{S}_{\Psi,r}$ can be computed as:

$$d\mathcal{S}_{\Psi,r}(R, F^{\mathbf{u}}) = -\left[\frac{\partial}{\partial F} \Psi(r(\mathbf{x}; R, F^{\mathbf{u}})) \right] \nabla F^{\mathbf{u}}(\mathbf{x}), \tag{3.16}$$

and for the brightness constancy constraint in particular, this derivation can be computed as:

$$d\mathcal{S}_{\Psi,r}(R, F^{\mathbf{u}}) = -[\nabla F^{\mathbf{u}}] \frac{d}{dr_{BC}} \Psi(r_{BC}(\mathbf{x}; R, F, \mathbf{u})) \tag{3.17}$$

Finally, we can rewrite Eq. (3.17) for the derivatives of the modified ℓ_1 norm and the ℓ_2 norm cases. These derivatives can be computed as:

$$d\mathcal{S}_{\ell_2}(R, F^{\mathbf{u}}) = -2(R(\mathbf{x}) - F^{\mathbf{u}}(\mathbf{x}))\nabla F^{\mathbf{u}}(\mathbf{x}) \tag{3.18}$$

$$d\mathcal{S}_{\text{mod}-\ell_1}(R, F^{\mathbf{u}}) = -\frac{R(\mathbf{x}) - F^{\mathbf{u}}(\mathbf{x})}{\sqrt{(R(\mathbf{x}) - F^{\mathbf{u}}(\mathbf{x}))^2 + \epsilon}} \nabla F^{\mathbf{u}}(\mathbf{x}) \tag{3.19}$$

3.2 Regularizers

If any of the dissimilarity measures are optimized with respect to a non parametric deformation field, there is no guarantee of a unique solution[12]. In fact, there are many solutions to the optimization problem which may not present continuity or smoothness. A regularization term must be added to the dissimilarity measure in order to force the non parametric registration problem being well-posed and having a smooth solution. In this thesis, we use two different regularizers for the cost function $E(R, F^{\mathbf{u}})$.

3.2.1 Diffusion Regularizer

The diffusion regularizer is defined as the gradient of the deformation field raised to the second power and it is designed to minimize large variations of the gradient of the deformation field:

$$\mathcal{R}_{\text{diff}}(\mathbf{u}) = \sum_{j=1}^{n} \|\nabla u_j\|^2 \ , \tag{3.20}$$

and its derivative with respect to the deformation field can be computed as the divergence of the gradient of the deformation field:

$$\frac{\partial \mathcal{R}_{\text{diff}}(\mathbf{u})}{\partial \mathbf{u}} = -\Delta \mathbf{u} \ , \tag{3.21}$$

with

$$\Delta \mathbf{u} = \nabla \cdot \nabla \mathbf{u}.$$

3.2.2 Modified ℓ_1 Norm Regularizer

First, we define what we call the ℓ_1 regularizer in order to impose sparsity on the gradient of th deformation field $\mathbf{u}$. The ℓ_1 regularizer can be constructed as the absolute value of the gradient of the deformation field:

$$\mathcal{R}_{\ell_1}(\mathbf{u}) = \sum_{j=1}^{n} |\nabla u_j| \ . \tag{3.22}$$

However, the ℓ_1 regularizer from Eq. (3.22) has the same problem regarding the ℓ_1 minimization as in Eq. (3.9) for the ℓ_1 norm dissimilarity measure; it is not differentiable everywhere. Modifying the ℓ_1 regularizer $\mathcal{R}_{\ell_1}$ as in Eq. (3.10), the modified ℓ_1 regularizer, which is differentiable everywhere, can be constructed as:

$$\mathcal{R}_{\text{mod}-\ell_1}(\mathbf{u}) = \sum_{j=1}^{n} \sqrt{(\nabla u_j)^2 + \epsilon} \ , \tag{3.23}$$

for $\epsilon \in \mathbb{R}^+$. The derivative of the modified ℓ_1 regularizer with respect to the deformation field can be computed as:

$$\frac{\partial \mathcal{R}_{\text{mod}-\ell_1}(\mathbf{u})}{\partial \mathbf{u}} = \frac{-\Delta \mathbf{u}}{\sqrt{(\nabla \mathbf{u})^2 + \epsilon}}, \tag{3.24}$$

which is the divergence of the gradient of the deformation field $\Delta \mathbf{u} = \nabla \cdot \nabla \mathbf{u}$, divided by the square root of the second power of the gradient of the deformation field plus the sparsity parameter ϵ.

3.3 Transformation Models

In this section, we describe three transformation models used in the experiments in Chapter 5. An affine transformation model which has few degrees of freedom is first described. For nonrigid registration, a dense deformation field transformation model is described. The second transformation model used is a non parametric dense deformation field transformation model and the last one is a parametric dense deformation field transformation model.

3.3.1 Affine

A classical family of geometrical transformations is the affine transformation model. The affine transformation consist of a combination of translations, rotations, scaling and skew [15, 16]. It includes rigid transformations which are made up from composing translations and rotations transformations only. Using the affine transformation model a point of coordinates x, y, z in the grid is mapped to another point x', y', z' by:

$$\begin{pmatrix} x' \\ y' \\ z' \end{pmatrix} = \begin{pmatrix} a_{11} & a_{12} & a_{13} \\ a_{21} & a_{22} & a_{23} \\ a_{31} & a_{32} & a_{33} \end{pmatrix} \cdot \begin{pmatrix} x \\ y \\ z \end{pmatrix} + \begin{pmatrix} t_0 \\ t_1 \\ t_2 \end{pmatrix} \tag{3.25}$$

The transformation (3.26) can be broken down to:

$$\begin{pmatrix} x' \\ y' \\ z' \end{pmatrix} = S \cdot R_X \cdot R_Y \cdot R_Z \cdot C \cdot \begin{pmatrix} x \\ y \\ z \end{pmatrix} + \begin{pmatrix} t_0 \\ t_1 \\ t_2 \end{pmatrix}, \tag{3.26}$$

where S stands for scaling matrix, R_X, R_Y and R_Z are rotation matrices around the X, Y and Z axes and C is a skew matrix.

In the affine transformation model case we do not need to add a regularization term $\mathcal{R}$ in the cost function $E(R, F^{\mathbf{u}})$ since this transformation model acts like a regularization itself. Hence, for the affine transformation model the registration problem is simplified as:

$$\min_{\mathbf{u}} \quad E(R, F^{\mathbf{u}}) = \min_{\mathbf{u}} \quad \mathcal{S}(R, F^{\mathbf{u}}). \tag{3.27}$$

Two of the registration algorithms that are used in the experiments in Chapter 5 were affine transformation models. The first one uses the ℓ_2 norm and the other one uses the modified ℓ_1 norm. In order to distinguish between different registration algorithms, the following notation is proposed:

$$\mathcal{A}^{\text{affine}}_{\ell_2} \rightarrow \min_{\mathbf{u}} \quad E(R, F) \quad = \quad \min_{\mathbf{u}} \quad \mathcal{S}_{\ell_2}(R, F) \tag{3.28}$$

$$\mathcal{A}^{\text{affine}}_{\text{mod}-\ell_1} \rightarrow \min_{\mathbf{u}} \quad E(R, F) \quad = \quad \min_{\mathbf{u}} \quad \mathcal{S}_{\text{mod}-\ell_1}(R, F), \tag{3.29}$$

where $\mathcal{A}$ denotes the algorithm to be used, the superscript denotes the transformation model used and the subscript indicates the dissimilarity measure between the images being registered.

3.3.2 Non Parametric Dense Deformation Field

For dense deformation field transformation models, we do not take into account a limited set of transformation parameters but a dense deformation field $\mathbf{u}$ instead. For

the nonrigid case, we do need a regularization term $\mathcal{R}$ in the cost function $E(R, F^{\mathbf{u}})$ since the transformation has many degrees of freedom and the problem is ill-posed.

The principle behind a variational analysis is to look for a deformation field $\mathbf{u}$ making the cost functional stationary [17]:

$$\left.\frac{\partial E(\mathbf{u}+h\mathbf{w})}{\partial h}\right|_{h=0} = 0, \quad \forall \mathbf{w} \tag{3.30}$$

where $\mathbf{w}$ is an arbitrary function belonging to the same space of continuous and differentiable functions as $\mathbf{u}$. In Eq.(3.30), h is a scalar factor multiplying the perturbation function $\mathbf{w}$.

Three of the registration algorithms that are used in the experiments in Chapter 5 are non parametric dense deformation field transformation models. Here, we combine the ℓ_2 norm and the modified ℓ_1 norm dissimilarity measures and the diffusion and the modified ℓ_1 regularizers. In order to distinguish between different registration algorithms, the following notation is used:

$$\mathcal{A}^{\text{non param}}_{\ell_2,\ \text{diff}} \quad \rightarrow \quad \min_{\mathbf{u}}\ E(R, F^{\mathbf{u}}) = \min_{\mathbf{u}}\ \mathcal{S}_{\ell_2}(R, F^{\mathbf{u}}) + \lambda \mathcal{R}_{\text{diff}}(\mathbf{u}) \tag{3.31}$$

$$\mathcal{A}^{\text{non param}}_{\text{mod}-\ell_1,\ \text{diff}} \quad \rightarrow \quad \min_{\mathbf{u}}\ E(R, F^{\mathbf{u}}) = \min_{\mathbf{u}}\ \mathcal{S}_{\text{mod}-\ell_1}(R, F^{\mathbf{u}}) + \lambda \mathcal{R}_{\text{diff}}(\mathbf{u}) \tag{3.32}$$

$$\mathcal{A}^{\text{non param}}_{\ell_2,\ \text{mod}-\ell_1} \quad \rightarrow \quad \min_{\mathbf{u}}\ E(R, F^{\mathbf{u}}) = \min_{\mathbf{u}}\ \mathcal{S}_{\ell_2}(R, F^{\mathbf{u}}) + \lambda \mathcal{R}_{\text{mod}-\ell_1}(\mathbf{u}), \tag{3.33}$$

where the superscript indicates that the transformation model used is the non parametric dense deformation field and the subscript indicates the dissimilarity measure between the images to be registered and the regularization strategy of the deformation field used.

3.3.3 Parametric Dense Deformation Field

In order to represent the space of allowed deformations during registration, a set of basis functions can be defined. The decomposition of the deformation field as a weighted sum of basis functions is a convenient way of modeling the deformation field[14, 18]. In this case, the deformation field $\mathbf{u}$ can be defined as a sum of basis functions weighted by some parameters:

$$u_w(x) = \sum_j w_j B_j(x), \tag{3.34}$$

where $B_j : \Omega^n \longrightarrow \mathbb{R}$ are the basis functions and $w_j \in \mathbb{R}$ are the parameters to be found.

In this thesis, Gaussian function are used as basis functions for the modeling of the deformation field. The Gaussian kernel is a subset of the more general radial basis functions [14]. For this case, we can rewrite Eq. (3.34) as:

$$u_i = \sum_j w_j \; exp\left(\frac{(x_i - x_j)^2}{2\sigma^2}\right), \tag{3.35}$$

where w_j are the kernel weights we want to find in the optimization step of the gradient descent method and σ is the standard deviation of the Gaussian distribution function. A sparse solution of the registration indicates that most of the weight parameters w_j are zero. The deformation is described by summation of only a few baseis functions.

The last three registration algorithms that are used in the experiments in Chapter 5 are dense deformation field transformation models with a Gaussian parameterization. Again, we combine the ℓ_2 norm and the modified ℓ_1 norm dissimilarity measures and the diffusion and modified ℓ_1 regularizers. In order to distinguish between different registration algorithms, the following notation is provided:

$$\mathcal{A}^{\text{param}}_{\ell_2,\ \text{diff}} \quad \rightarrow \quad \min_{\mathbf{u}} \; E(R, F^{\mathbf{u}}) = \min_{\mathbf{u}} \; \mathcal{S}_{\ell_2}(R, F^{\mathbf{u}}) + \lambda \mathcal{R}_{\text{diff}}(\mathbf{u}) \tag{3.36}$$

$$\mathcal{A}^{\text{param}}_{\text{mod}-\ell_1,\ \text{diff}} \quad \rightarrow \quad \min_{\mathbf{u}} \; E(R, F^{\mathbf{u}}) = \min_{\mathbf{u}} \; \mathcal{S}_{\text{mod}-\ell_1}(R, F^{\mathbf{u}}) + \lambda \mathcal{R}_{\text{diff}}(\mathbf{u}) \tag{3.37}$$

$$\mathcal{A}^{\text{param}}_{\ell_2,\ \text{mod}-\ell_1} \quad \rightarrow \quad \min_{\mathbf{u}} \; E(R, F^{\mathbf{u}}) = \min_{\mathbf{u}} \; \mathcal{S}_{\ell_2}(R, F^{\mathbf{u}}) + \lambda \mathcal{R}_{\text{mod}-\ell_1}(\mathbf{u}), \tag{3.38}$$

where the superscript indicates that the transformation model used is the non parametric dense deformation field and the subscript indicates the dissimilarity measure between the images to be registered and the regularization strategy of the deformation field used.

Derivative of the Energy Function to the Parameter Set

During the optimization step, we need to compute the derivative of the cost functional with respect to the parameter set at each iteration. Consider the easy case of the ℓ_2 norm dissimilarity measure with no regularization term:

$$E(R, F^{\mathbf{u}}) = \sum (R(\mathbf{x}) - F^{\mathbf{u}}(\mathbf{x}))^2. \tag{3.39}$$

Applying the chain rule, the derivative of the Eq. (3.39) with respect to the deformation field (3.35) can be expanded as:

$$\frac{dE}{dw_j} \;=\; \sum_i \frac{dE}{du_i}\,\frac{du_i}{dw_j} \;= \tag{3.40}$$

$$\;=\; -2\sum_i (R(\mathbf{x}) - F^{\mathbf{u}}(\mathbf{x}))\;\frac{dF^{\mathbf{u}}(\mathbf{x})}{du_i}\;exp\left(\frac{(x_i - x_j)^2}{2\sigma^2}\right). \tag{3.41}$$

In order to reduce the computational time of this calculation, another sub sampling factor is introduced in the algorithm, reducing the number of Gaussian functions to be placed in the grid.

3.4 Optimization Strategy

For the simulations done in Chapter 5, a gradient descent minimization strategy is chosen. First, the floating image is resampled on the new grid defined by the parameter set. After that, the gradient of the energy cost function to the parameter set is calculated. Then, a step proportional to the negative of the gradient is taken and, finally, the parameter set is updated. We repeat this procedure at each iteration until a fixed number of iterations is reached. Furthermore, the step size τ is a fixed value.

$$\mathbf{u}_{k+1} = \mathbf{u}_k - \tau \cdot \frac{\partial E}{\partial \mathbf{u}}. \tag{3.42}$$

The necessary derivatives for the minimization process are detailed in Eqs. (3.18) and (3.19) for the dissimilarity measure term and in Eqs. (3.21) and (3.24) for the regularization term.

3.5 Validation

In general, nonrigid registration is a highly ill-posed problem. Therefore, two different registration methods may provide similar image matching with qualitatively different transformations. In this work we evaluated the local and global dissimilarities existing between the obtained deformation field after registration and the ground truth. These two validation measures are proposed in [19]. The local differences between both deformation fields are quantified from the distance between the associated Jacobian matrices J. The Jacobian matrix of the deformation field is defined by:

$$J = \begin{pmatrix} \partial(x-u_x)/\partial x & \partial(x-u_x)/\partial y & \partial(x-u_x)/\partial z \\ \partial(x-u_y)/\partial x & \partial(x-u_y)/\partial y & \partial(x-u_y)/\partial z \\ \partial(x-u_z)/\partial x & \partial(x-u_z)/\partial y & \partial(x-u_z)/\partial z \end{pmatrix} \tag{3.43}$$

A distance defined on the group of symmetric positive definite matrices Sym^+ applied to the strain matrix $S = (J^T \cdot J)^{1/2}$ is used:

$$d_{\mathrm{J}}(S_1, S_2) = \sqrt{trace(log(S_1^{-1/2} S_2 S_1^{-1/2})^2)}. \tag{3.44}$$

Complementing this local dissimilarity measure between deformation fields, we also measure the global differences between corresponding grid points in both deformation fields:

$$d_{\mathrm{SSD}}(\varphi_1(x,y,z),\varphi_2(x,y,z)) = \sqrt{(x_1-x_2)^2+(y_1-y_2)^2+(z_1-z_2)^2}, \qquad (3.45)$$

where $\varphi_1(x,y,z) = (x_1,y_1,z_1)$ and $\varphi_2(x,y,z) = (x_2,y_2,z_2)$.

Chapter 4

Materials

In this thesis, registration of brain tumor MR images are studied. For the evaluation of the registration algorithms in the presence of a tumor, two different cases are considered. The first one is the deformation of brain tissue due to tumor mass effect or volume expansion and the second one is the infiltration of brain tissue by tumor or edema. Edema appears around tumor mainly in the white matter regions and may also contain infiltrative tumor cells.

4.1 Data

The methods are tested on simulated MR images of the brain that were generated by the BrainWeb [20, 21, 22]. In total, five healthy subjects were studied (subjects 04, 06, 20, 38 and 52). The images used have an isotropic voxel size of 1mm $\times$ 1mm $\times$ 1mm. In the discrete domain, these images are 256$\times$256$\times$181 pixels long. Due to time constraints, an axial slice was selected from each image volume and the study of the algorithms was conducted in the 2D case. The axial slice selected is slice 90.

A skull stripping operation was done as a preprocessing step with a brain extraction tool from MIPAV software [23, 24]. The parameters used are the ones that follow: 3 iterations and a Gaussian standard deviation of 0.5 voxels for filtering the image to remove irregularities, a kernel size of 0.64 voxels to detect image edges, 1 iteration to isolate the brain through morphological erosion and 7.0 mm kernel diameter in order to perform surface cleanup and image masking. Careful parameter selection is necessary for the brain extraction algorithm to produce a good outcome. Figure 4.1 shows the intermediate images of the skull stripping process. Small errors in the brain extraction are not believed to have an impact on the final result.

In order to simulate a tumor expansion between two different scans of the same patient, we use data from tumorSim software [25, 26]. The software combines physical and statistical modeling to generate synthetic multi-modal 3D brain MRI with tumor and edema. The data consist of two discrete images of a simulated brain image with

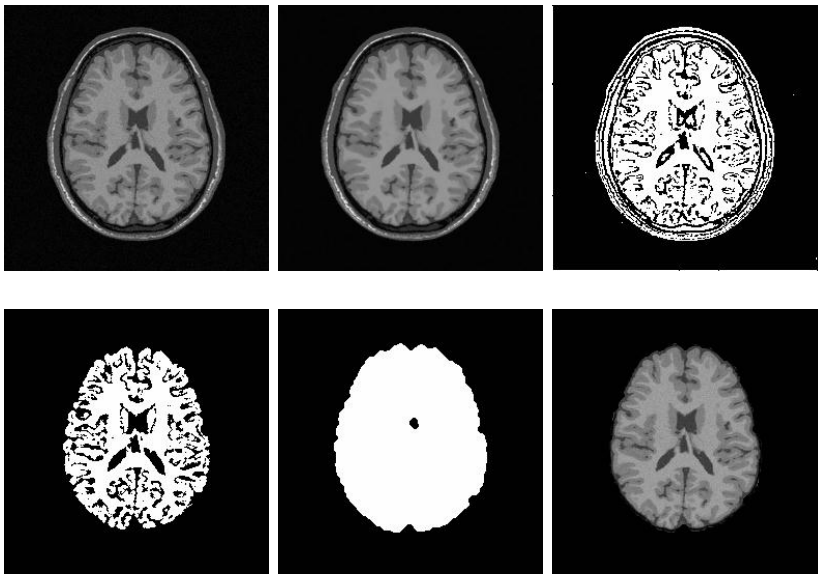

Figure 4.1: Skull stripping: intermediate images. In the first row: the original image (left), the filtered image (middle) and the edge image mask (right). In the second row: the isolated brain mask (left), the brain mask after applying morphological erosion (middle) and the extracted brain image (right).

a pathology. We use three different tumors that vary from one another in size and shape. We will simulate tumor deformations and we will apply them to the five healthy subjects in different locations. The registration process will try to recover those deformations.

4.2 Ground Truth

In order to provide objective assessments of registration performance, there is a need for an objective ground truth to systematically compare different methodologies. Depending on whether we consider the tumor mass effect or the tumor infiltration case, the ground truth generation process will be different. This process is detailed in this section and it is repeated for each subject.

Tumor Deformation Generation

For the registration of the tumor, a deformation field that represents a local expansion in the grid has to be generated. To that end, we derive a normal distribution in 2D:

$$u(x_1, x_2) = \frac{1}{\sigma\sqrt{2\pi}}\ exp\left(\frac{(x_1-\mu_1)^2 + (x_2-\mu_2)^2}{2\sigma^2}\right) \tag{4.1}$$

$$\tag{4.2}$$

$$\nabla u(x_1, x_2) = (\frac{\partial u}{\partial x_1}, \frac{\partial u}{\partial x_2}), \tag{4.3}$$

where

$$\frac{\partial u}{\partial x_1} = \frac{-x_1}{\sigma^3\sqrt{2\pi}}\, exp\left(-\frac{(x_1-\mu_1)^2+(x_2-\mu_2)^2}{2\sigma^2}\right) \tag{4.4}$$

$$\frac{\partial u}{\partial x_2} = \frac{-x_2}{\sigma^3\sqrt{2\pi}}\, exp\left(-\frac{(x_1-\mu_1)^2+(x_2-\mu_2)^2}{2\sigma^2}\right), \tag{4.5}$$

where (x_1, x_2) are grid coordinates, (μ_1, μ_2) is the point in the grid where the expansion is generated, u is the deformation field and σ is the bandwith of the normal distribution.

Each of these derivatives generates two forces in opposites directions in their domains. The local deformation is generated by adding the identity transform to these derivatives to place the simulated expansion on a grid. Figure 4.2 shows this grid expansion. Through the σ parameter and the magnitude of the normal distribution, different expansions can be generated.

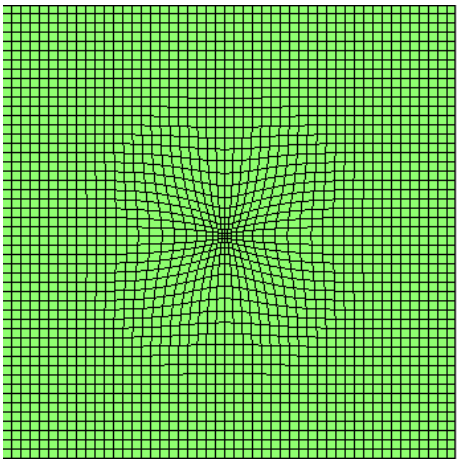

Figure 4.2: Generation of a local expansion in a deformation field.

4.2.1 Mass Effect

A simple tumor mass effect ground truth generation process is illustrated in Figure 4.3. The discrete ground truth image is loaded and the corresponding tumor is picked. Then, the tumor is placed in the healthy brain within a realistic intensity value taking into consideration the surrounding tissues. At the same time, an expansion deformation field is simulated at the tumor location and, finally, the healthy brain is resampled with the tumor in it with the generated deformation field. Some assumptions were made in the mass effect simulation process. For instance, the tumor intensity is homogeneous throughout the tissue and both floating and reference

images taken at two different time points have the same tumor grey value.

Figure 4.3 illustrates the process just described, where the input images for each registration algorithm described in Chapter 3 are generated.

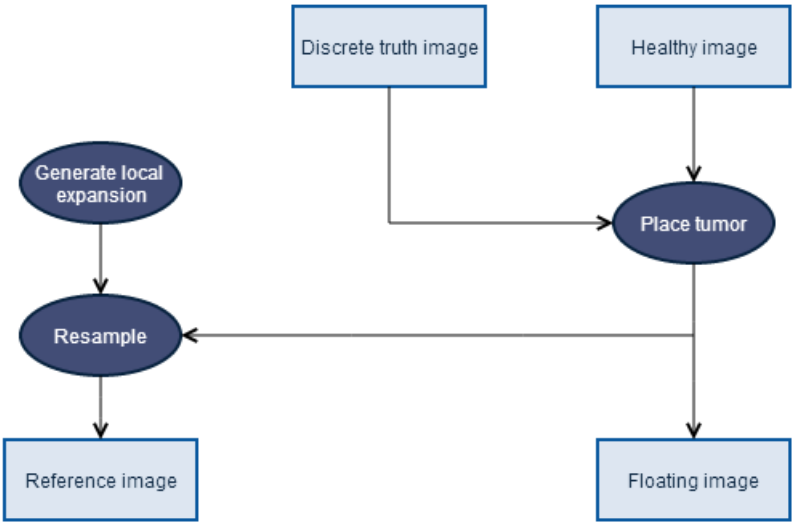

Figure 4.3: Ground truth generation process for mass effect

In addition, the deformation field ground truth is known in order to validate the performance of different registration algorithms. Figure 4.4 shows the floating image, the ground truth deformation field generated and the reference image. The growing tumor is shown in Figure 4.4 along with other nearby tissues being pushed by the tumor expansion.

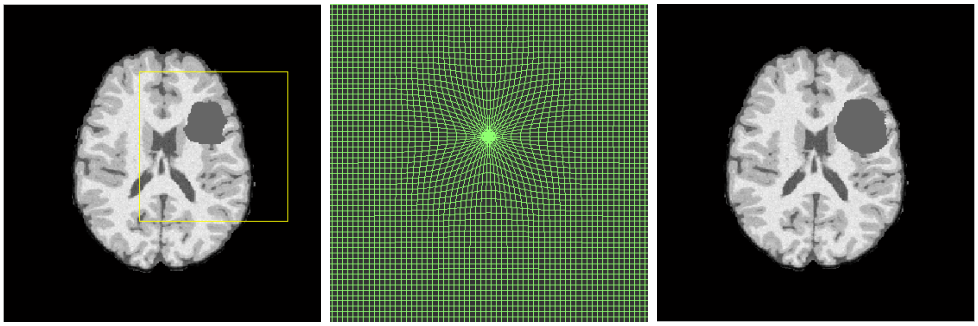

Figure 4.4: Intermediate images in the mass effect ground truth generation process From left to right: the floating image with the pathology (left), the ground truth deformation field generated (middle) and the reference image with the tumor mass effect (right). The yellow square in the first image indicates the location in which the second image is zoomed.

4.2.2 Tumor Infiltration

Similarly, the tumor infiltration ground truth can be generated. In this case, instead of resampling the healthy brain image with the tumor in it, only the tumor itself is resampled with the corresponding generated deformation field. Then, both the initial tumor and the expanded tumor are placed in the healthy brain image. Figure 4.4 illustrates the process of ground truth generation for the infiltration case. The floating image is the healthy brain with the tumor in it and the reference image is the healthy brain with the expanded tumor in it, so that the healthy tissue remains untouched. Notice that for the infiltration case, the ground truth is not the generated expansion deformation field as in the mass effect case, but the identity transform since we expect all of the brain tissues will remain in their location.

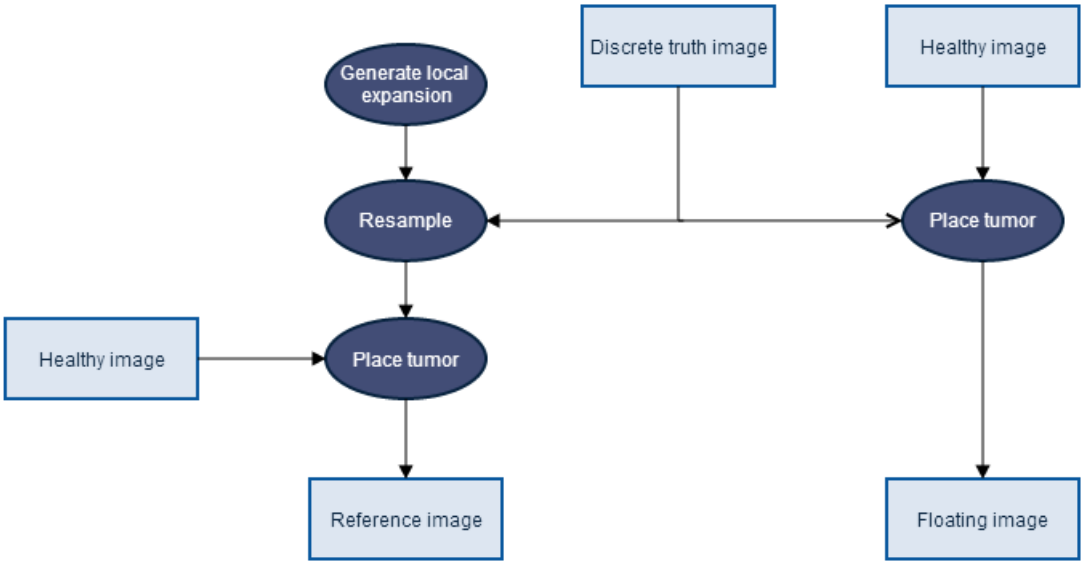

Figure 4.5: Ground truth generation process for tumor infiltration

Figure 4.6 shows an example of the intermediate images of the process illustrated in Figure 4.5:

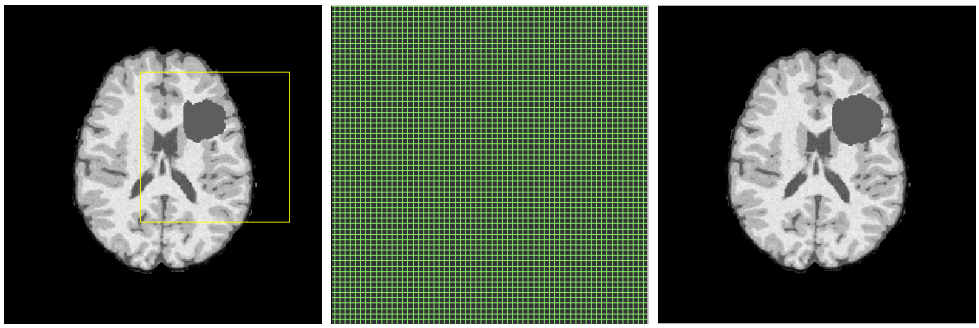

Figure 4.6: Intermediate images in the infiltration ground truth generation process From left to right: the floating image with the pathology (left), the ground truth deformation field generated (middle) and the reference image with the tumor infiltration (right).

Chapter 5

Experiments

The performance of the eight algorithms described in Chapter 3 is tested in MR images where a pathology is present. For this purpose, we set up some experiments that will allow us to assess whether or not incorporating sparsity in the registration problem can be useful in practice.

5.1 Experiment 1: Parameter Tuning

Each algorithm is tested in all five subjects. For the tumor mass effect data set and the tumor infiltration data set, the parameters of the algorithms are tuned beforehand. This tuning reveals that the most relevant parameters are the regularization parameter λ, for the dense deformation field transformation models, and the standard deviation σ for the parametric dense deformation field transformation model. Other parameters like the sparsity parameter ϵ, the value of the step size τ in the gradient descent and the number of iterations have a limited influence on the results. The sparsity parameter ϵ is set up to $1.0e^{-3}$ in all the algorithms in order for the modified ℓ_1 norm to behave similarly to the ℓ_1 norm as seen in Chapter 3. The step size and number of iterations are also fixed parameters. For the parametric dense deformation field algorithms, step size is $\tau = 1$ and the number of iterations 300. For the non parametric dense deformation field algorithms, step size is $\tau = 10$ and the number of iterations 500.

The parameter selection for the parametric and non parametric dense deformation field algorithms are shown in Table 5.1 for the tumor mass effect and in Table 5.2 for the tumor infiltration. For the parametric dense deformation field algorithms, simulations are done with different combinations of λ and σ parameters. For the non parametric dense deformation field algorithms only different values of the regularization parameter λ are studied. For the affine transformation model algorithms, no parameter tuning is required. The selection criteria of the parameters is a mix between a quantitative validation of the registration by computing the d_{SSD} and d_J distances between deformation fields and a qualitative validation by visual assessment of the deformation field obtained. The complete study can be found in

the Appendix.

5.1.1 Tumor Mass Effect

Table 5.1 shows the selected λ and σ parameters of the eight algorithms described in the methods in Chapter 3, for the tumor mass effect subjects:

	Subject 04	Subject 06	Subject 20	Subject 38	Subject 52
$\mathcal{A}^{\text{param}}_{\ell_2,\ \text{diff}}$	$\lambda = 1.0e^2$ $\sigma = 6.0$	$\lambda = 1.0e^2$ $\sigma = 4.0$	$\lambda = 1.0e^2$ $\sigma = 4.0$	$\lambda = 1.0e^2$ $\sigma = 4.0$	$\lambda = 1.0e^2$ $\sigma = 4.0$
$\mathcal{A}^{\text{param}}_{\text{mod}-\ell_1,\ \text{diff}}$	$\lambda = 1.0e^2$ $\sigma = 4.0$	$\lambda = 1.0e^2$ $\sigma = 4.0$	$\lambda = 1.0e^2$ $\sigma = 4.0$	$\lambda = 1.0e^2$ $\sigma = 4.0$	$\lambda = 1.0e^2$ $\sigma = 4.0$
$\mathcal{A}^{\text{param}}_{\ell_2,\ \text{mod}-\ell_1}$	$\lambda = 1.0e^2$ $\sigma = 8.0$	$\lambda = 1.0e^2$ $\sigma = 6.0$	$\lambda = 1.0e^2$ $\sigma = 6.0$	$\lambda = 1.0e^2$ $\sigma = 6.0$	$\lambda = 1.0e^2$ $\sigma = 6.0$
$\mathcal{A}^{\text{non param}}_{\ell_2,\ \text{diff}}$	$\lambda = 1.0e^3$	$\lambda = 1.0e^3$	$\lambda = 1.0e^3$	$\lambda = 1.0e^3$	$\lambda = 1.0e^3$
$\mathcal{A}^{\text{non param}}_{\text{mod}-\ell_1,\ \text{diff}}$	$\lambda = 1.0e^2$	$\lambda = 1.0e^2$	$\lambda = 1.0e^2$	$\lambda = 1.0e^2$	$\lambda = 1.0e^2$
$\mathcal{A}^{\text{non param}}_{\ell_2,\ \text{mod}-\ell_1}$	$\lambda = 1.0e^3$	$\lambda = 1.0e^3$	$\lambda = 1.0e^3$	$\lambda = 1.0e^3$	$\lambda = 1.0e^3$

Table 5.1: Parameter selection for the algorithms tested in the tumor mass effect subjects.

5.1.2 Tumor Infiltration

Table 5.2 shows the selected λ and σ parameters of the eight algorithms described in the methods in Chapter 3, for the tumor infiltration subjects:

	Subject 04	Subject 06	Subject 20	Subject 38	Subject 52
$\mathcal{A}^{\text{param}}_{\ell_2,\ \text{diff}}$	$\lambda = 1.0e^2$ $\sigma = 4.0$	$\lambda = 1.0e^2$ $\sigma = 4.0$	$\lambda = 1.0e^2$ $\sigma = 4.0$	$\lambda = 1.0e^2$ $\sigma = 4.0$	$\lambda = 1.0e^2$ $\sigma = 2.0$
$\mathcal{A}^{\text{param}}_{\text{mod}-\ell_1,\ \text{diff}}$	$\lambda = 1.0e^2$ $\sigma = 4.0$	$\lambda = 1.0e^2$ $\sigma = 4.0$	$\lambda = 1.0e^2$ $\sigma = 6.0$	$\lambda = 1.0e^2$ $\sigma = 4.0$	$\lambda = 1.0e^2$ $\sigma = 4.0$
$\mathcal{A}^{\text{param}}_{\ell_2,\ \text{mod}-\ell_1}$	$\lambda = 1.0e^2$ $\sigma = 4.0$	$\lambda = 1.0e^2$ $\sigma = 6.0$	$\lambda = 1.0e^2$ $\sigma = 4.0$	$\lambda = 1.0e^2$ $\sigma = 6.0$	$\lambda = 1.0e^2$ $\sigma = 4.0$
$\mathcal{A}^{\text{non param}}_{\ell_2,\ \text{diff}}$	$\lambda = 1.0e^3$	$\lambda = 1.0e^3$	$\lambda = 1.0e^3$	$\lambda = 1.0e^3$	$\lambda = 1.0e^3$
$\mathcal{A}^{\text{non param}}_{\text{mod}-\ell_1,\ \text{diff}}$	$\lambda = 1.0e^2$	$\lambda = 1.0e^2$	$\lambda = 1.0e^2$	$\lambda = 1.0e^2$	$\lambda = 1.0e^2$
$\mathcal{A}^{\text{non param}}_{\ell_2,\ \text{mod}-\ell_1}$	$\lambda = 1.0e^3$	$\lambda = 1.0e^3$	$\lambda = 1.0e^3$	$\lambda = 1.0e^3$	$\lambda = 1.0e^3$

Table 5.2: Parameter selection for the algorithms tested in the tumor infiltration subjects.

5.2 Experiment 2: Tumor Mass Effect

We proceed by registering the five subjects with a tumor mass effect and the five subjects with tumor infiltration and study the registration algorithms' performance. The registration parameters used in this section are shown in Tables 5.1 and 5.2 in the previous section.

Table 5.3 shows the results for all the algorithms described in Chapter 3. In this table, distances d_{SSD} and d_J between the deformation fields before and after registration are shown (mean ± standard deviation) for the tumor mass effect data set. Table 5.3 indicates that the parametric dense deformation field algorithms perform better than the non parametric dense deformation field algorithms in this setting. The smallest distances come from the algorithms $\mathcal{A}^{\text{param}}_{\ell_2,\ \text{diff}}$, $\mathcal{A}^{\text{param}}_{\ell_2,\ \text{mod}-\ell_1}$ and $\mathcal{A}^{\text{non param}}_{\ell_2,\ \text{diff}}$, while algorithms such us $\mathcal{A}^{\text{param}}_{\text{mod}-\ell_1,\ \text{diff}}$ and $\mathcal{A}^{\text{non param}}_{\text{mod}-\ell_1,\ \text{diff}}$ that use the modified ℓ_1 norm in the dissimilarity measure have larger distances, in overall. The affine registration algorithms have the same mean and standard deviation for both the ℓ_2 norm and the modified ℓ_1 norm.

	Subject 04	Subject 06	Subject 20	Subject 38	Subject 52
$\mathcal{A}^{\text{param}}_{\ell_2,\ \text{diff}}$	**0.1049 ± 0.6891**	**0.1276 ± 0.8027**	**0.0882 ± 0.5823**	**0.1399 ± 0.7848**	**0.1504 ± 0.8698**
	0.0251 ± 0.1878	**0.0350 ± 0.2297**	**0.0247 ± 0.1765**	**0.0351 ± 0.2412**	**0.0354 ± 0.2266**
$\mathcal{A}^{\text{param}}_{\text{mod}-\ell_1,\ \text{diff}}$	0.1501 ± 0.8867	0.1577 ± 0.9130	0.1094 ± 0.6465	0.1476 ± 0.7629	0.1737 ± 0.9081
	0.3510 ± 0.2248	0.0386 ± 0.2408	0.0282 ± 0.1852	0.0365 ± 0.2459	0.0385 ± 0.2339
$\mathcal{A}^{\text{param}}_{\ell_2,\ \text{mod}-\ell_1}$	**0.1322 ± 0.6741**	**0.1252 ± 0.5978**	**0.0848 ± 0.4454**	**0.1469 ± 0.7460**	**0.1528 ± 0.7840**
	0.0268 ± 0.2006	**0.0293 ± 0.1768**	**0.0217 ± 0.1441**	**0.0335 ± 0.2174**	**0.0312 ± 0.1916**
$\mathcal{A}^{\text{non param}}_{\ell_2,\ \text{diff}}$	**0.1464 ± 0.9399**	**0.1409 ± 0.9222**	**0.0883 ± 0.6725**	**0.1292 ± 0.7905**	**0.1621 ± 0.9443**
	0.0332 ± 0.2312	**0.0340 ± 0.2361**	**0.0237 ± 0.1857**	**0.0320 ± 0.2448**	**0.0349 ± 0.2358**
$\mathcal{A}^{\text{non param}}_{\text{mod}-\ell_1,\ \text{diff}}$	0.2264 ± 1.2294	0.2176 ± 1.2031	0.1251 ± 0.8094	0.1735 ± 0.9138	0.2120 ± 1.1150
	0.0482 ± 0.2530	0.0472 ± 0.2557	0.0341 ± 0.1990	0.0440 ± 0.2567	0.0472 ± 0.2504
$\mathcal{A}^{\text{non param}}_{\ell_2,\ \text{mod}-\ell_1}$	0.1925 ± 1.1054	0.1794 ± 1.0745	0.1052 ± 0.7500	0.1498 ± 0.8597	0.1862 ± 1.0461
	0.0420 ± 0.2668	0.0424 ± 0.2724	0.0258 ± 0.1963	0.0370 ± 0.2647	0.0394 ± 0.2566
$\mathcal{A}^{\text{affine}}_{\ell_2}$	0.2630 ± 1.3566	0.2630 ± 1.3566	0.1395 ± 0.8864	0.1972 ± 1.0175	0.2367 ± 1.2209
	0.0433 ± 0.2579	0.0433 ± 0.2579	0.0281 ± 0.1994	0.0374 ± 0.2591	0.0412 ± 0.2538
$\mathcal{A}^{\text{affine}}_{\text{mod}-\ell_1}$	0.2630 ± 1.3566	0.2630 ± 1.3566	0.1395 ± 0.8864	0.1972 ± 1.0175	0.2367 ± 1.2209
	0.0433 ± 0.2579	0.0433 ± 0.2579	0.0281 ± 0.1994	0.0374 ± 0.2591	0.0412 ± 0.2538

Table 5.3: Registration evaluations of the tumor mass effect data set. The first row in each algorithm is for the global d_{SSD} distance and the second row is for the local d_{J} distance.

Figure 5.1 illustrates the tumor mass effect images for the study in Table 5.3: the floating image, the reference image, the ground truth deformation field and the final deformation field after registration for the $\mathcal{A}^{\text{non param}}_{\ell_2,\ \text{diff}}$, as an example. Subjects 04, 06, 20, 38 and 52 are displayed from top to bottom.

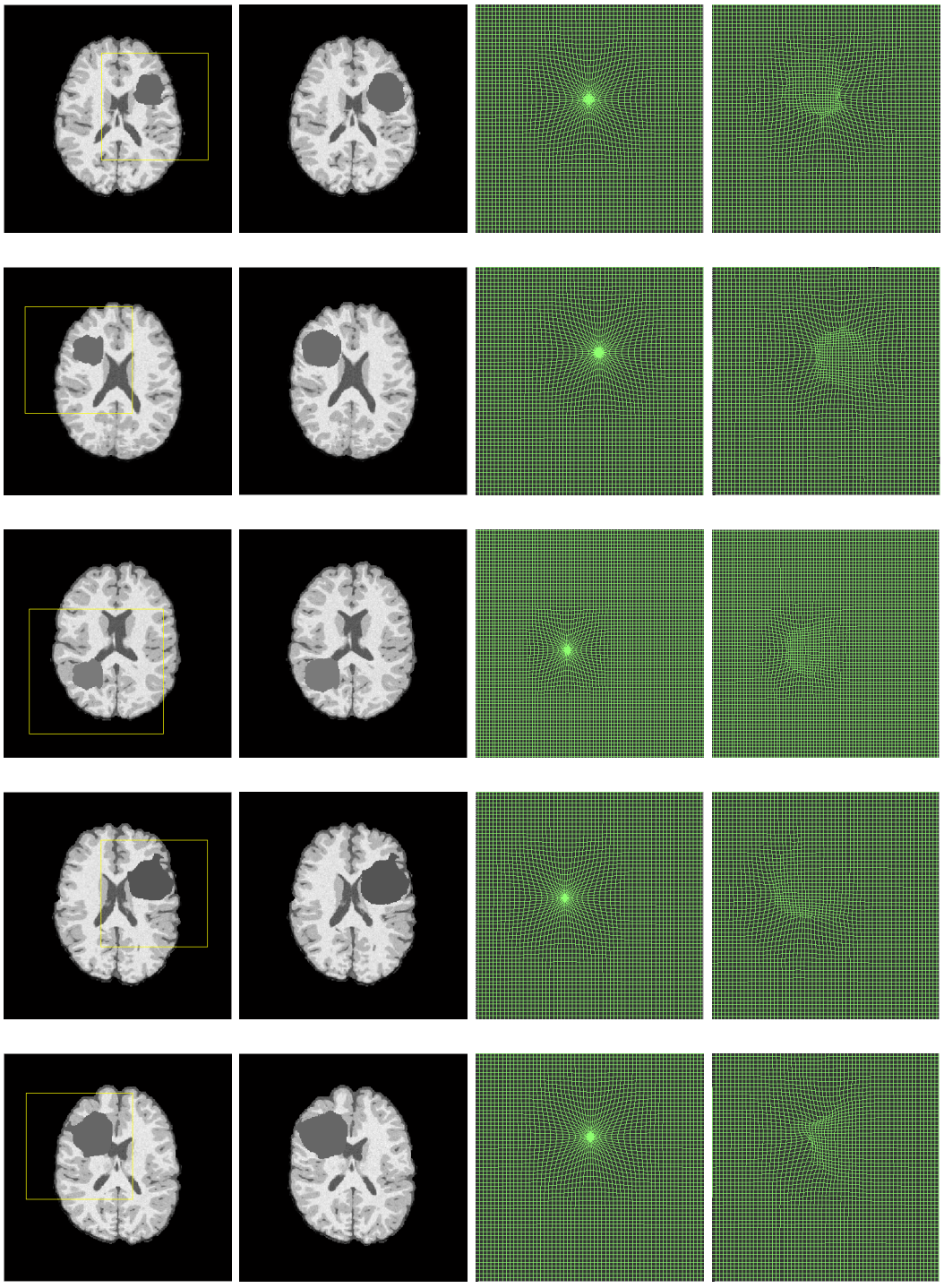

Figure 5.1: Tumor mass effect data set input images. From left to right: floating image, reference image, ground truth deformation field and deformation field after registration. Subjects 04, 06, 20, 38 and 52 are displayed from top to bottom.

Figure 5.2 shows the initial and final overlap between the two floating and reference image of subject 20 for the $\mathcal{A}^{\text{param}}_{\ell_2,\ \text{diff}}$, $\mathcal{A}^{\text{param}}_{\ell_2,\ \text{mod}-\ell_1}$ and $\mathcal{A}^{\text{non param}}_{\ell_2,\ \text{diff}}$ registration algorithms.

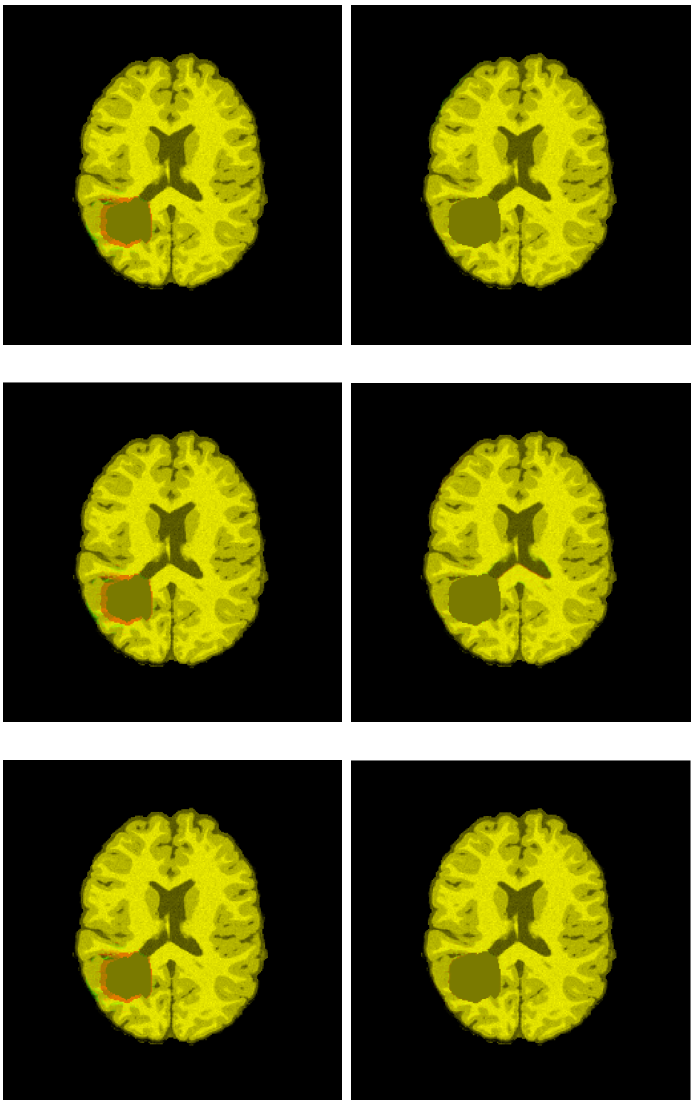

Figure 5.2: In columns, the initial overlap image and the final overlap image. In rows, visual assessment of $\mathcal{A}^{\text{param}}_{\ell_2,\ \text{diff}}$, $\mathcal{A}^{\text{param}}_{\ell_2,\ \text{mod}-\ell_1}$ and $\mathcal{A}^{\text{non param}}_{\ell_2,\ \text{diff}}$ registration algorithms.

Figure 5.3 shows the intensity difference image between the floating and the reference image, before and after registration. It also shows the deformation fields, before and after registration for the same subject 20 and same algorithms $\mathcal{A}^{\text{param}}_{\ell_2,\ \text{diff}}$, $\mathcal{A}^{\text{param}}_{\ell_2,\ \text{mod}-\ell_1}$ and $\mathcal{A}^{\text{non param}}_{\ell_2,\ \text{diff}}$, as in Figure 5.2:

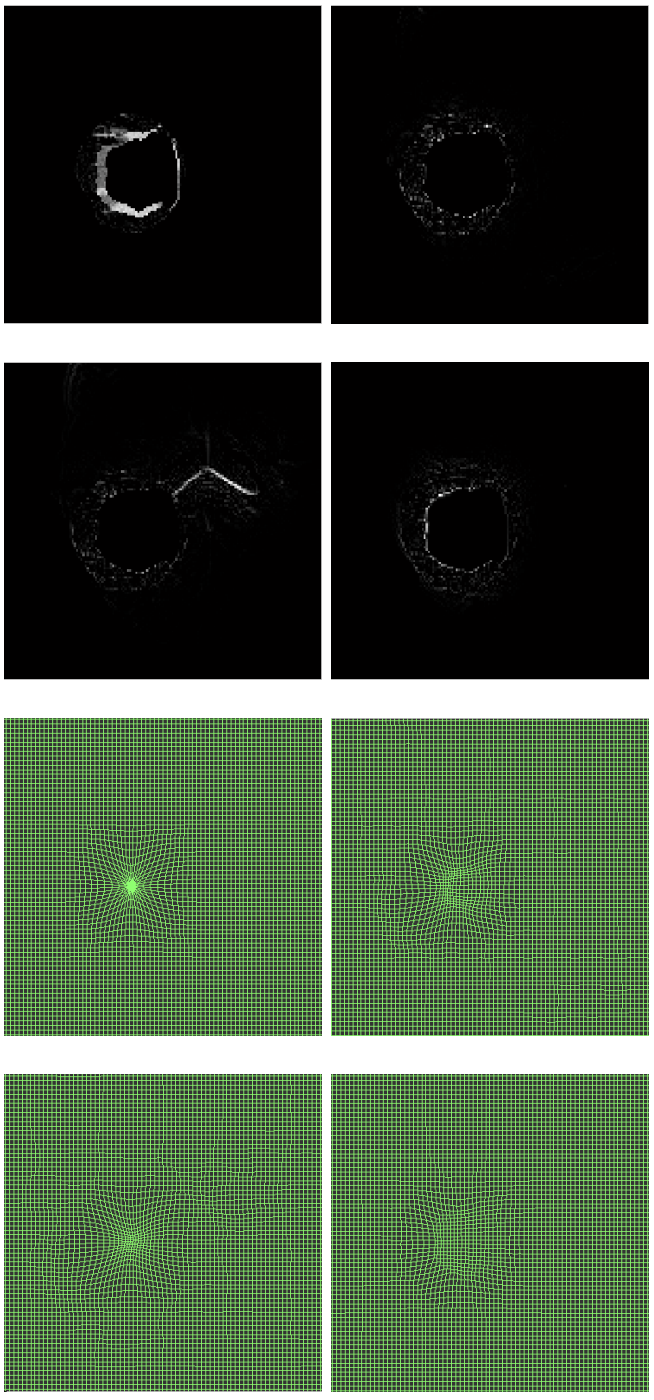

Figure 5.3: Rows 1 and 2: intensity difference image. Rows 3 and 4: deformation fields. First image in rows 1 and 3 shows the initial floating image case. Then, algorithms $\mathcal{A}^{\text{param}}_{\ell_2,\ \text{diff}}$, $\mathcal{A}^{\text{param}}_{\ell_2,\ \text{mod}-\ell_1}$ and $\mathcal{A}^{\text{non param}}_{\ell_2,\ \text{diff}}$ are displayed in order.

In Figure 5.3, some differences between the three algorithms occur. Algorithm $\mathcal{A}^{\text{param}}_{\ell_2,\ \text{mod}-\ell_1}$ recovers the deformation around the pathology slightly better than the other two algorithms, but misregistration errors appear in areas where no deformation was simulated in the first place. Precisely, it generates a secondary deformation near the ventricles. This effect is not an expected result but the visual assessment of the registration is really good, overall. Both algorithms $\mathcal{A}^{\text{param}}_{\ell_2,\ \text{diff}}$ and $\mathcal{A}^{\text{non param}}_{\ell_2,\ \text{diff}}$ perform quite similar for the tumor mass effect case.

Figure 5.4 shows the performance of the modified ℓ_1 norm as dissimilarity measure. In particular, it shows the overlap images of the algorithms $\mathcal{A}^{\text{param}}_{\text{mod}-\ell_1,\ \text{diff}}$ and $\mathcal{A}^{\text{non param}}_{\text{mod}-\ell_1,\ \text{diff}}$ before and after registering subject 38:

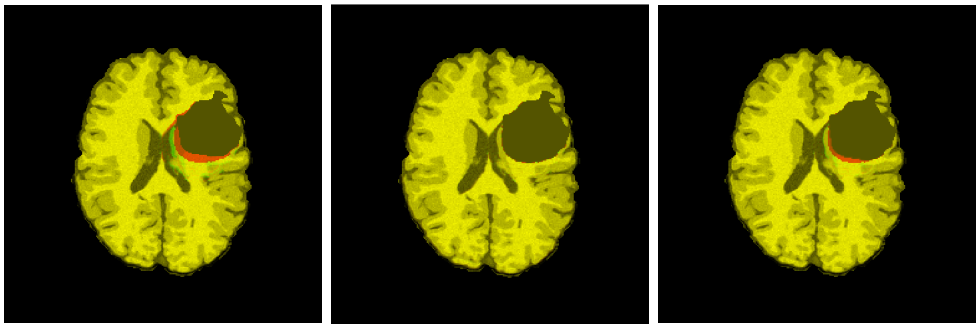

Figure 5.4: Visual assessment of $\mathcal{A}^{\text{param}}_{\text{mod}-\ell_1,\ \text{diff}}$ and $\mathcal{A}^{\text{non param}}_{\text{mod}-\ell_1,\ \text{diff}}$ algorithms. In columns, the overlap image before registration, the final overlap image using $\mathcal{A}^{\text{param}}_{\text{mod}-\ell_1,\ \text{diff}}$ algorithm, and the final overlap image using $\mathcal{A}^{\text{non param}}_{\text{mod}-\ell_1,\ \text{diff}}$ algorithm.

Figure 5.5 shows the intensity difference image and the deformation fields before (ground truth) and after registration of subject 38, for the $\mathcal{A}^{\text{param}}_{\text{mod}-\ell_1,\ \text{diff}}$ and $\mathcal{A}^{\text{non param}}_{\text{mod}-\ell_1,\ \text{diff}}$. In Figure 5.4, we appreciate a good registration of the tumor for the parametric dense deformation field, but the deformation field itself seems slightly regularized in Figure 5.5. Whereas the non parametric dense deformation field algorithm do not recover the tumor at all. Associated with Table 5.3, the results provided by algorithm $\mathcal{A}^{\text{non param}}_{\text{mod}-\ell_1,\ \text{diff}}$ are the worst results for the dense deformation field transformation model algorithms together with the affine transformation model algorithms.

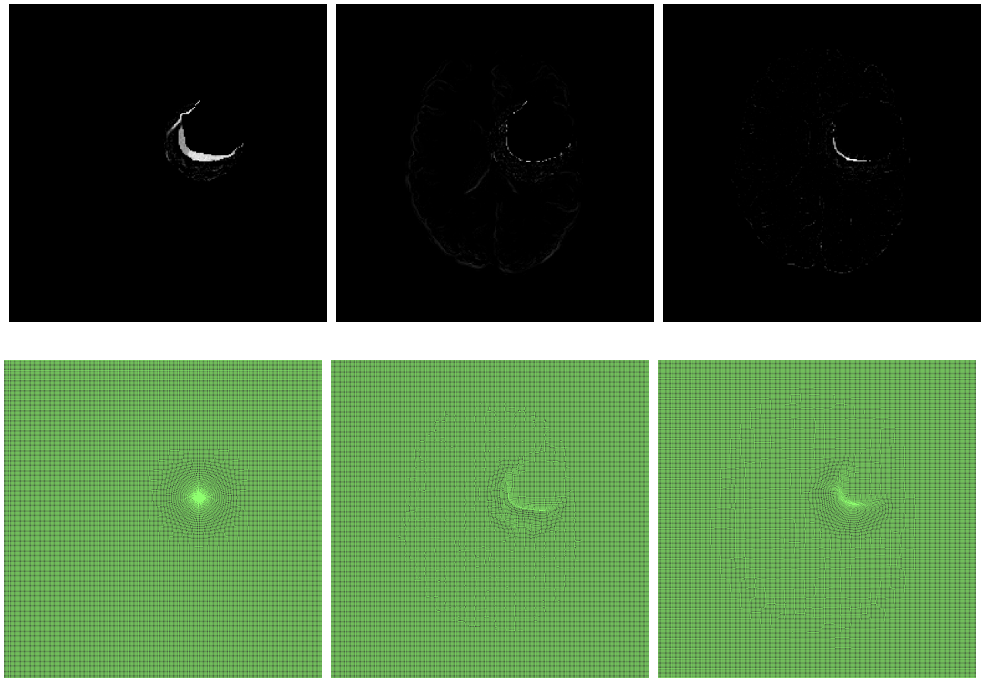

Figure 5.5: Visual assessment of $\mathcal{A}^{\text{param}}_{\text{mod}-\ell_1,\ \text{diff}}$ and $\mathcal{A}^{\text{non param}}_{\text{mod}-\ell_1,\ \text{diff}}$ registration algorithms. First row shows the intensity difference image before (column 1) and after registration (columns 2 and 3). Second row shows the ground truth deformation field (column 1) and the deformation field after registration (columns 2 and 3.

5.3 Experiment 3: Tumor Infiltration

Table 5.4. shows the results for all the algorithms described in Chapter 3. In this table, distances d_{SSD} and d_{J} between the deformation fields before and after registration are shown (mean ± standard deviation) for the tumor infiltration data set. Overall, the results are smaller than the results obtained in the tumor mass effect case, since the comparison of the deformation is done with the identity transform deformation field. $\mathcal{A}^{\text{non param}}_{\ell_2,\ \text{diff}}$ and $\mathcal{A}^{\text{non param}}_{\ell_2,\ \text{mod}-\ell_1}$ algorithms perform better than the rest. $\mathcal{A}^{\text{param}}_{\ell_2,\ \text{diff}}$ and $\mathcal{A}^{\text{param}}_{\text{mod}-\ell_1,\ \text{diff}}$ algorithms recover the transformation good enough but their performance is slightly worst then the previous two algorithms. The affine transformation model registration algorithms have distances d_{SSD} and d_{J} equal to zero. However, for the affine case, the performance of the registration is not good since we can not recover the deformation.

	Subject 04	Subject 06	Subject 20	Subject 38	Subject 52
$\mathcal{A}^{\text{param}}_{\ell_2,\ \text{diff}}$	0.1262 ± 0.7216	0.0908 ± 0.5398	0.1162 ± 0.8687	0.0803 ± 0.5729	0.0246 ± 0.2768
	0.0308 ± 0.1717	0.0210 ± 0.1130	0.0295 ± 0.2183	0.0193 ± 0.1352	0.0097 ± 0.0998
$\mathcal{A}^{\text{param}}_{\text{mod}-\ell_1,\ \text{diff}}$	0.1073 ± 0.4977	0.0803 ± 0.3765	0.1866 ± 0.8715	0.0775 ± 0.4242	0.0589 ± 0.2805
	0.0202 ± 0.0805	0.0160 ± 0.0628	0.0311 ± 0.1713	0.0152 ± 0.0714	0.0120 ± 0.0491
$\mathcal{A}^{\text{param}}_{\ell_2,\ \text{mod}-\ell_1}$	0.1406 ± 0.7855	0.1547 ± 0.7074	0.1705 ± 0.9855	0.1357 ± 0.7544	0.1234 ± 0.4980
	0.0364 ± 0.1991	0.0321 ± 0.1723	0.0488 ± 1.0680	0.0253 ± 0.1218	0.0410 ± 0.1389
$\mathcal{A}^{\text{non param}}_{\ell_2,\ \text{diff}}$	**0.0752 ± 0.4111**	**0.0474 ± 0.3088**	**0.0783 ± 0.5669**	**0.0518 ± 0.3845**	**0.0263 ± 0.2157**
	0.0127 ± 0.0632	**0.0084 ± 0.0492**	**0.0135 ± 0.0862**	**0.0085 ± 0.0548**	**0.0049 ± 0.0361**
$\mathcal{A}^{\text{non param}}_{\text{mod}-\ell_1,\ \text{diff}}$	0.0340 ± 0.1838	0.0270 ± 0.1527	0.0222 ± 0.1367	0.0208 ± 0.1172	0.0177 ± 0.0897
	0.0149 ± 0.0485	0.0124 ± 0.0395	0.0120 ± 0.0381	0.0120 ± 0.0357	0.0110 ± 0.0298
$\mathcal{A}^{\text{non param}}_{\ell_2,\ \text{mod}-\ell_1}$	**0.0579 ± 0.3234**	**0.0398 ± 0.2535**	**0.0463 ± 0.4007**	**0.0351 ± 0.2806**	**0.0029 ± 0.1780**
	0.0128 ± 0.0827	**0.0083 ± 0.0560**	**0.0128 ± 0.1213**	**0.0080 ± 0.0754**	**0.0045 ± 0.0416**
$\mathcal{A}^{\text{affine}}_{\ell_2}$	0.0000 ± 0.0000	0.0000 ± 0.0000	0.0000 ± 0.0000	0.0000 ± 0.0000	0.0000 ± 0.0000
	0.0000 ± 0.0000	0.0000 ± 0.0000	0.0000 ± 0.0000	0.0000 ± 0.0000	0.0000 ± 0.0000
$\mathcal{A}^{\text{affine}}_{\text{mod}-\ell_1}$	0.0000 ± 0.0000	0.0000 ± 0.0000	0.0000 ± 0.0000	0.0000 ± 0.0000	0.0000 ± 0.0000
	0.0000 ± 0.0000	0.0000 ± 0.0000	0.0000 ± 0.0000	0.0000 ± 0.0000	0.0000 ± 0.0000

Table 5.4: Registration evaluations of the tumor infiltration data set. The first row in each algorithm is for the global d_{SSD} distance and the second row is for the local d_{J} distance.

Figure 5.6 illustrates the tumor infiltration images for the study in Table 5.4: the floating image, the reference image, the ground truth deformation field and the final deformation field after registration for the $\mathcal{A}^{\text{non param}}_{\ell_2,\ \text{diff}}$ algorithm, as an example. Subjects 04, 06, 20, 38 and 52 are displayed from top to bottom. Notice that for the infiltration case, the ground truth deformation field is the identity transform since we expect the healthy tissue to remain in the same voxels.

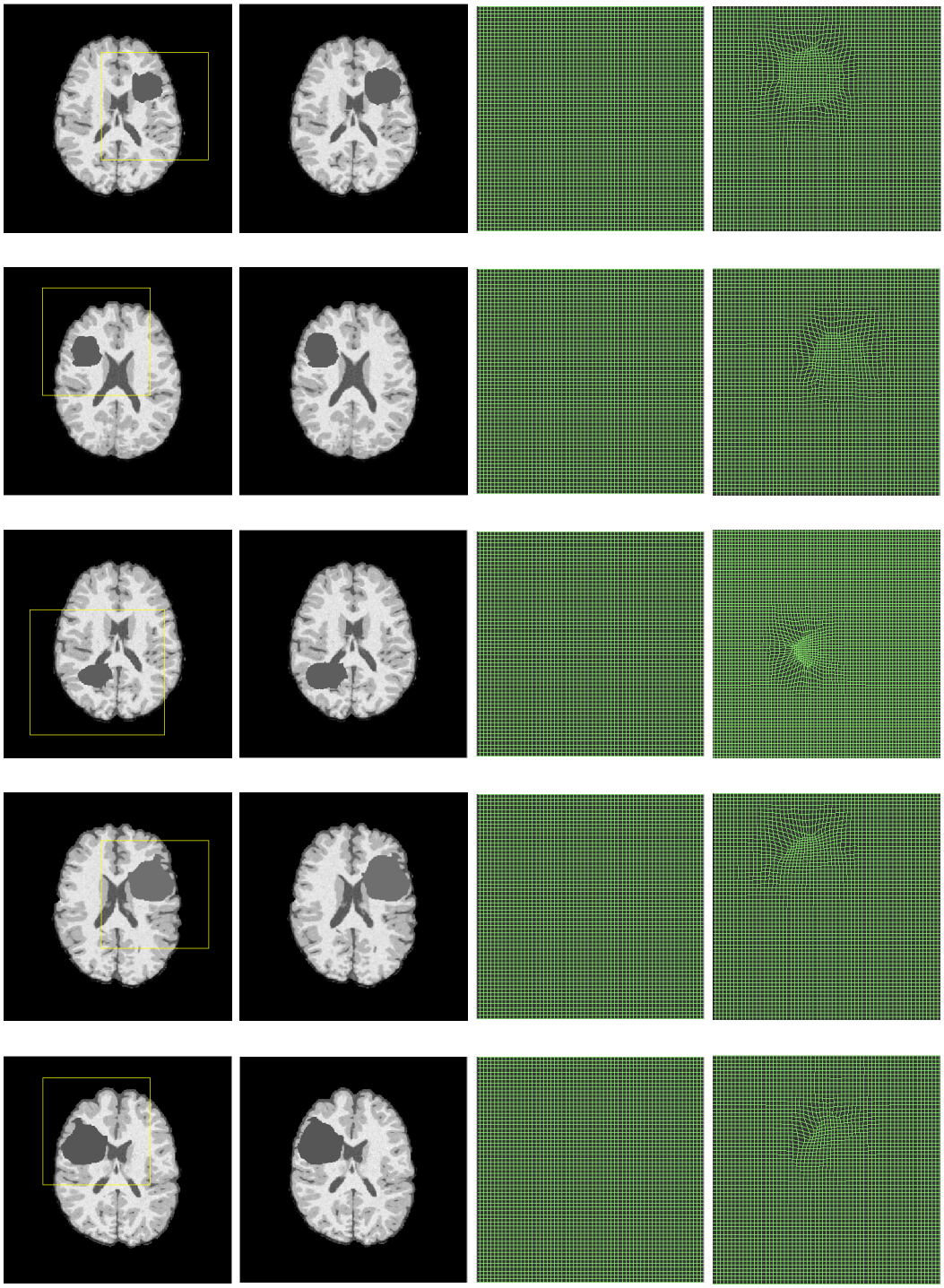

Figure 5.6: Tumor infiltration data set input images. In columns, floating image, reference image, ground truth deformation field and deformation field after registration. Subjects 04, 06, 20, 38 and 52 are displayed from top to bottom.

Figure 5.7 shows the initial and final overlap between the two floating and reference image of subject 20 for the $\mathcal{A}^{\text{non param}}_{\ell_2,\ \text{diff}}$, $\mathcal{A}^{\text{non param}}_{\ell_2,\ \text{mod}-\ell_1}$ and $\mathcal{A}^{\text{param}}_{\ell_2,\ \text{diff}}$ registration algorithms.

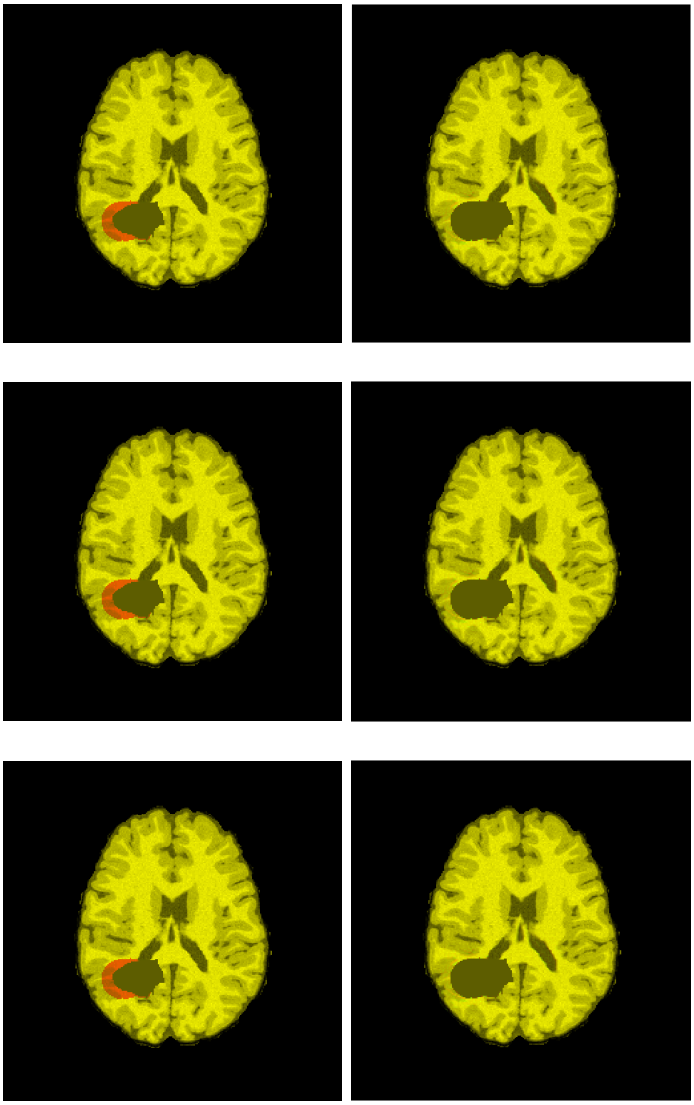

Figure 5.7: In columns, the initial overlap image, and the final overlap images. In rows, visual assessment of $\mathcal{A}^{\text{non param}}_{\ell_2,\ \text{diff}}$, $\mathcal{A}^{\text{non param}}_{\ell_2,\ \text{mod}-\ell_1}$ and $\mathcal{A}^{\text{param}}_{\ell_2,\ \text{diff}}$.

Figure 5.8 shows the intensity difference images between the floating and the reference image, before and after registration. It also shows the deformation fields, before and after registration for the same subject 20 but for algorithms $\mathcal{A}^{\text{param}}_{\ell_2,\ \text{diff}}$, $\mathcal{A}^{\text{param}}_{\ell_2,\ \text{mod}-\ell_1}$ and $\mathcal{A}^{\text{non param}}_{\ell_2,\ \text{diff}}$. Notice that for the parametric dense deformation field algorithms, a secondary deformation appears in a location not near the pathology

location. This effect is not as expected.

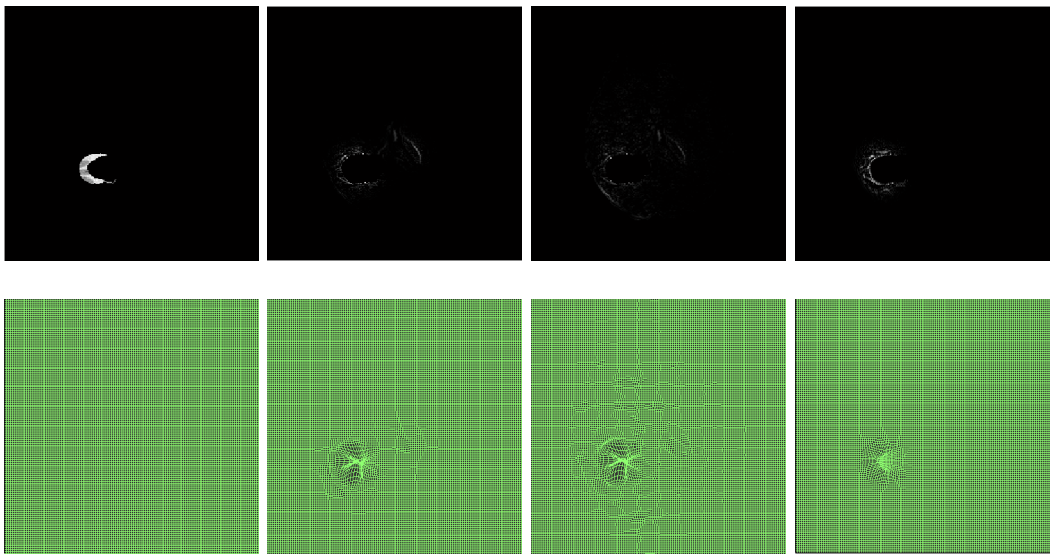

Figure 5.8: Visual assessment of $\mathcal{A}^{\text{param}}_{\ell_2,\ \text{diff}}$, $\mathcal{A}^{\text{param}}_{\ell_2,\ \text{mod}-\ell_1}$ and $\mathcal{A}^{\text{non param}}_{\ell_2,\ \text{diff}}$ registration algorithms. First row shows the intensity difference image before (column 1) and after registration (columns 2, 3 and 4). Second row shows the ground truth deformation field (column 1) and the deformation field after registration (columns 2, 3 and 4).

Figure 5.9 shows the performance of the modified ℓ_1 norm as dissimilarity measure for the tumor infiltration data set. In particular, it shows the overlap images of the algorithms $\mathcal{A}^{\text{param}}_{\text{mod}-\ell_1,\ \text{diff}}$ and $\mathcal{A}^{\text{non param}}_{\text{mod}-\ell_1,\ \text{diff}}$ before and after registering subject 38:

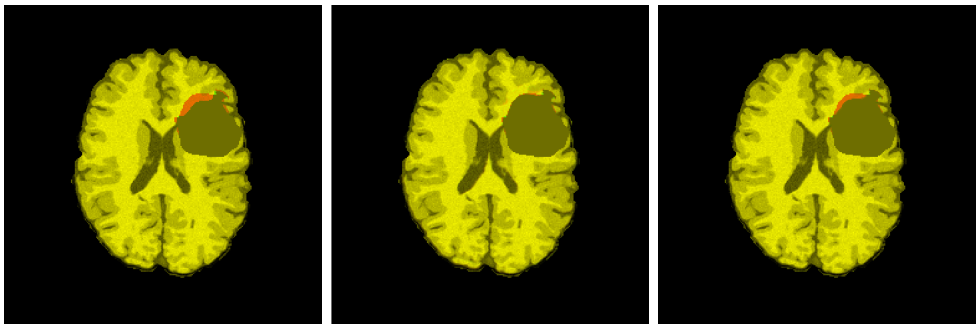

Figure 5.9: Visual assessment of $\mathcal{A}^{\text{param}}_{\text{mod}-\ell_1,\ \text{diff}}$ and $\mathcal{A}^{\text{non param}}_{\text{mod}-\ell_1,\ \text{diff}}$ algorithms. In columns, the overlap image before registration, the final overlap image using $\mathcal{A}^{\text{param}}_{\text{mod}-\ell_1,\ \text{diff}}$ algorithm, and the final overlap image using $\mathcal{A}^{\text{non param}}_{\text{mod}-\ell_1,\ \text{diff}}$ algorithm.

Figure 5.10 shows the intensity difference image and the deformation fields before (ground truth) and after registration of subject 38, for the $\mathcal{A}^{\text{param}}_{\text{mod}-\ell_1,\ \text{diff}}$ and $\mathcal{A}^{\text{non param}}_{\text{mod}-\ell_1,\ \text{diff}}$:

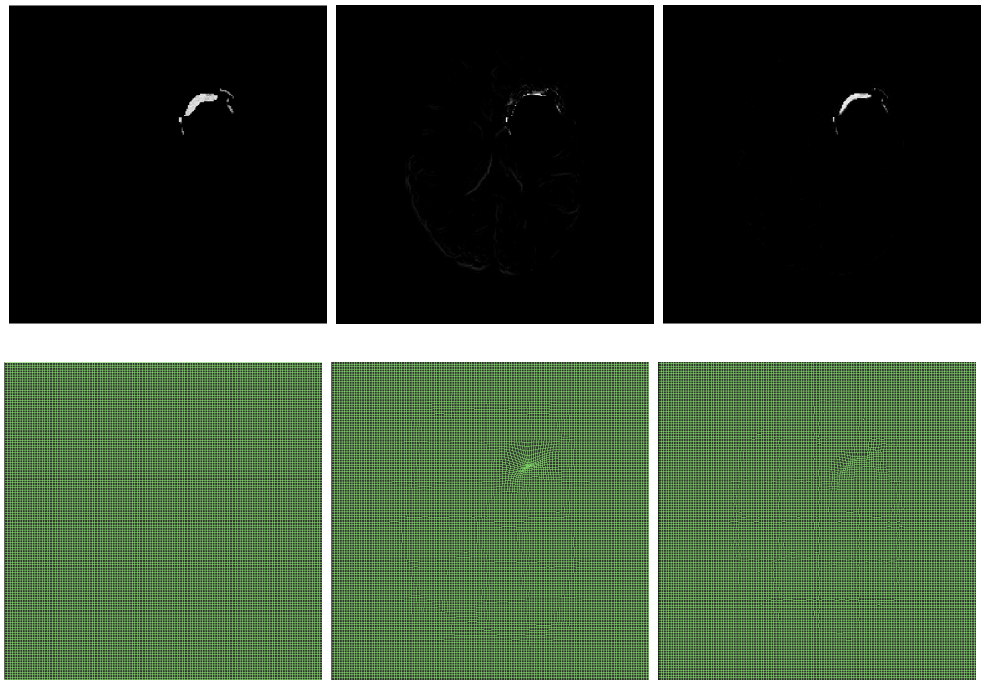

Figure 5.10: Visual assessment of $\mathcal{A}^{\text{param}}_{\text{mod}-\ell_1,\ \text{diff}}$ and $\mathcal{A}^{\text{non param}}_{\text{mod}-\ell_1,\ \text{diff}}$ registration algorithms. First row shows the intensity difference image before (column 1) and after registration (columns 2 and 3). Second row shows the ground truth deformation field (column 1) and the deformation field after registration (columns 2 and 3).

Chapter 6

Discussion and Future Work

In this thesis, we presented a theoretical and experimental comparison of eight registration algorithms. Each algorithm uses different transformation models as well as dissimilarity measures and regularization strategies. We analyzed differences in these elements within the registration for brain MR images where a pathology is present. In particular, we focused on two different cases: pathologies due to tumor mass effect and due to tumor infiltration. We also studied the influence of the regularization parameter in each algorithm and compared the performance of the registration algorithms. For all the algorithms, we considered a gradient descent optimization scheme.

In the first experiment, a tuning of the registration parameters was done for each of the algorithms described in the methods. The tuned regularization parameter was the same for all the parametric dense deformation field transformation model algorithms, given a fixed step size for the gradient descent optimization scheme and for a given number of iterations. The standard deviation of the parameterization depended on the magnitude of the simulated expansion. Hence, for larger deformations, one should increase the standard deviation of the Gaussian distribution. For the non parametric dense deformation field, one should lower the regularization parameter just for the algorithm that uses the modified ℓ_1 norm as dissimilarity measure.

For the tumor mass effect and tumor infiltration experiments we can state that, for the algorithms that do recover the deformation, the ones that use a parametric dense deformation field transformation model perform better when recovering large deformations. On the other hand, algorithms that use a non parametric dense deformation field transformation model perform better when recovering smaller deformations, overall. In general, algorithms that use the ℓ_2 norm and a diffusion regularizer perform quite nice in both situations. Also, algorithms that use the modified ℓ_1 regularizer (parametric dense deformation field transformation model for the tumor mass effect case and non parametric dense deformation field transformation model for the tumor infiltration case) recover the deformation where the tumor expansion was generated but they also introduce additional large deformations in

other locations of the brain. Specifically, these additional deformations are generated near the edge of the brain surface or around the ventricles, in the middle. They are not random locations for the deformation to appear. These locations have similar intensity value than the tumor intensity value: black in the background and similar intensity value to the generated tumor intensity value, at the ventricles. That is due regularization techniques impose smoothness in the MR image by penalizing large changes in intensity between neighboring voxels.

There is a large difference in the performance of the modified ℓ_1 norm as dissimilarity measure between the parametric dense deformation field transformation model algorithm and the non parametric one. I have not come up with a reasonable explanation for this effect, but it is present in both the tumor mass effect experiment and the tumor infiltration experiment. It may be due the contribution of the additional terms that the modified ℓ_1 norm introduces in the cost function when computing the derivatives of the dissimilarity measure to the transformation parameters.

Both affine algorithms have the same distances between the deformation obtained and the ground truth. They both recover a deformation which is the identity transform deformation field. This is due most of the brain tissue is mapped onto each other and only small voxels differ from each other in the neighborhood of the tumor. Any affine transformation will generate more voxels not corresponded in the first iteration of the optimization problem and will not recover the deformation. Furthermore, results show affine transformation model algorithms have the largest distances when comparing this deformation with the ground truth for the tumor mass effect. On the other hand, for the tumor infiltration experiment, we notice that affine transformation model algorithms have distances equal to zero, instead. However, by no means this indicates a perfect registration. Again, affine transformation model algorithms do not recover the deformation, as in the mass effect experiment, and the optimal deformation that these algorithms will find is the identity transform deformation. But since we are comparing this deformation field obtained with the identity transform deformation field as ground truth, the distances are zero. Similarly, dense deformation field transformation model algorithms that do not recover the deformation have small d_{SSD} and d_J distances. On the same lines, algorithms that do recover most of the tumor expansion have larger d_{SSD} and d_J distances since the validation of the deformation field obtained is with the identity transform deformation field.

6.1 Future Work

Due time constraints, several improvements and suggestions can be made for the near future.

Simulation improvements

Within this thesis, several assumptions were made in the simulation of the data and the ground truth. We first removed the skull from the equation in order to make the problem easier to tackle. By leaving the skull in its place in a real setting, we could use some additional constraints that model a local rigidity of the deformation as in [29]. This penalty term would also be useful for the registration of pre-operative and intra-operative images in case an artifacts are introduced by the opening of the skull [17]. It could also be used for the registration of lung MR images. Other strategies for constructing penalty terms are described in [12, 30]. Another assumption relating the tumor tissue intensity value was made during the tumor simulation. We opted to model the tumor as an homogeneous tissue but in reality there may be different intensities for the tumor cells, pushing nearby tissue in various directions. Furthermore, tumor in both scans usually do not have the same intensity value, as we considered. Moreover, we also explored tumor mass effect and tumor infiltration separately but in reality both effects are present at the same time and they are not regarded separately. Other methods have been used for the generation of a realistic ground truth such us using biomechanical linear elastic finite model to simulate tumor mass effect [25] and a reaction-diffusion model [32] to simulate the infiltration by pathological cells or fluid.

3D Testing

Methods were tested on a 2D axial slice for each subject and results may not be representetive enough. For a complete validation, one should study the 3D real case in order to see whether the tumor is well recovered in other planes. By adding the third plane in the registration problem, not only it would turn the problem onto a harder computational problem since more voxels have to be taken into account when computing the intensity difference between the images being registered, but also for the calculations of the gradient in the differential partial equations. In the same way, for the parametric dense deformation field transformation model, more kernel functions have to be placed on the 3D grid. We already had to incorporate a subsampling factor in this algorithm in order to reduce the computational time of the calculation of the energy function derivative to the parameter set. In the 3D case might take too much effort to do these calculations. In order to tackle this issue, calculations could be done on a GPU (Graphics Processing Unit) to reduce the computational time of GPU and CPU communications [27]. In [28], a multiresolution optimization strategy is used and that it results to be efficient with respect to computational time and robustness.

Evaluation on larger data sets

In the setting studied, only five different subjects were considered. The results may not be representative enough. Besides that, the differences between each subject were small. We don't even considered other effects such us motion of the head of the

patient nor noise; only the deformation of a pathology. Making these changes may reveal additional results.

Test other settings

For a complete study of the methodologies presented, one should test the algorithms presented in other settings. We have already mentioned additional settings that could be tested in this Chapter. Apart from those, registration of breast MR images can be done by using free-form deformations based on B-splines to recover the motion and deformation of the breast itself [**?**]. Free-form deformations are also used in [33] to recover motion of the brain relative to the skull. These are just a few examples among others.

Chapter 7

Conclusions

It was the objective of this thesis to incorporate sparsity into the registration problem. In this work, this goal has been accomplished by using a modified ℓ_1 norm as dissimilarity measure, and by constructing a modified ℓ_1 regularizer for the minimization of a cost function in an optimization problem in order to recover a deformation field that anatomically maps two images of the same patient. We described eight different algorithms that combine these contributions with an ℓ_2 norm dissimilarity measure and diffusion regularizer. Three different transformation models are considered. The methods presented have been tested on simulated brain tumor MR images and validated by computing a dissimilarity metric between deformation fields.

Results show that algorithms that use the modified ℓ_1 regularizer and an ℓ_2 dissimilarity measure recover the deformation of the tumor, while the algorithm that uses the modified ℓ_1 norm dissimilarity measure along with a parametric dense deformation field transformation model recovers the deformation for large tumor expansions.

Bibliography

[1] Donoho, D. Compressed Sensing, *IEEE Transactions on Information Theory*, vol. 52, no. 4, pp. 1289-1306, 2006.

[2] E. Cand'es and J. Romberg. Quantitative robust uncertainty principles and optimally sparse decompositions. To appear in Foundations of Comput. Math., 2005.

[3] E. Candès, J. Romberg, and T. Tao. Robust uncertainty principles: Exact signal reconstruction from highly incomplete frequency information. *IEEE Trans. Inform. Theory*, June 2004. Available on theArXiV preprint server: `math.GM/0409186`.

[4] E. Candes and J. Romberg, ℓ_1-MAGIC : Recovery of Sparse Signals via Convex Programming, `http://www.acm.caltech.edu/l1magic/`, Oct 2005.

[5] M. Lustig , D. Donoho and J. Pauly. Sparse MRI: The Application of Compressed Sensing for Rapid MR Imaging, 2007 [online] Available: `http://www.stanford.edu/ mlustig/SparseMRI.pdf`

[6] M, Unser. Wavelets, sparsity and biomedical image reconstruction. EPFL, Lausanne, Switzerland, 2012. Available: `http://bigwww.epfl.ch/tutorials/unser_wavelets_sparsity2012.pdf`.

[7] A. Aldroubi and M. Unser. Wavelets in Medicine and Biology, 1996.

[8] K. L. Kroeker. Face recognition breakthrough, *Commun. ACM*, vol. 52, no. 8, pages 18-19, 2009.

[9] Philip Breen, Algorithms for Sparse Approximation, School of Mathematics, University of Edinburgh, 2009.

[10] S. Chen, D. L. Donoho, and M. A. Saunders. Atomic decomposition by basis pursuit, *SIAM J. Sci Comp.*, vol. 20, no. 1, pages 33-61, 1999.

[11] B. Fischer and J. Modersitzki, Ill-posed medicine. An introduction to image registration, *Inverse Problems*, 24 , 034008, 2008.

[12] Cahill, N.D.: Constructing and Solving Variational Image Registration Problems. D.Phil. Thesis, Department of Engineering Science, University of Oxford, 2009.

[13] J.M. Fitzpatrick, D.L.G. Hill and C.R. Maurer. Image Registration,Handbook of Medical Imaging. *Volume 2: Medical Image Processing and Analysis*, pages. 447-513, 2000.

[14] Zikic, D. Overview of Intensity-based Deformable Registration. *Computer Aided Medical Procedures (CAMP)*. MICCAI 2010. Retrieved from: `http://campar.in.tum.de/twiki/pub/DefRegTutorial/`

[15] Ashburner, J., Friston, K. Rigid body registration. In R. S. J. Frackowiak, K. Friston, C. Frith, R. Dolan, C. J. Price, S. Zeki, J. Ashburner (Eds.), *Human brain function* (2nd ed., pp. xvi, 1144 p.). Amsterdam; Boston: Elsevier Academic Press, 2003.

[16] J. West et al., Comparison and evaluation of retrospective intermodality brain image registration techniques, *Journal of Computer Assisted Tomography*, pp. 554-566, 1997.

[17] M. D. Craene. Dense Deformation Field Estimation for Pairwise and Multi-subjects Registration. , Universite Catholique de Louvain, B - 1348 Louvain-la-Neuve Belgique, Aug 2005.

[18] G. K. Rohde , A. Aldroubi and B. M. Dawant. The adaptive bases algorithm for intensity-based nonrigid image registration. *IEEE Trans. Med. Imag.*, vol. 22, no. 11, pp.1470-1479, 2003.

[19] M. Hernandez, Variational techniques with applications to segmentation and registration of medical images. PhD. Thesis, *Aragon Institude on Engineering Research (I3A)*, University of Zaragoza, 2008.

[20] C. A. Cocosco, V. Kollokian, R. L.-S. Kwan, and A. C. Evans, BrainWeb: Online interface to a 3D MRI simulated brain database, *NeuroImage*, vol. 5, no. 4 pt 2/4 S425, 1997. Available: `http://www.bic.mni.mcgill.ca/brainweb/`

[21] R. K.-S. Kwan, A. C. Evans, and G. B. Pike, An extensible MRI simulator for post-processing evaluation, *Proc. Visualization in Biomedical Computing - VBC'96* (Lecture Notes in Computer Science). Berlin, Germany: Springer-Verlag, 1996, vol. 1131, pages 135-140.

[22] D. L. Collins, A. P. Zijdenbos, V. Kollokian, J. G. Sled, N. J. Kabani, C. J. Holmes, and A. C. Evans, Design and construction of a realistic digital brain phantom, *IEEE Trans. Med. Imag.*, vol. 17, pages 463-468, June 1998.

[23] A. I. Scher, E. S. C. Korf, S. W. Hartley, L. J. Launer. An Epidemiologic Approach to Automatic Post-Processing of Brain MRI.

[24] David W. Shattuck, Stephanie R. Sandor-Leahy, Kirt A. Schaper, David A. Rottenburg, Richard M. Leahy. Magnetic Resonance Image Tissue Classification Using a Partial Volume Model. *NeuroImage*, pp. 856-876, 2001.

[25] Prastawa M, Bullitt E, Gerig G, Simulation of Brain Tumors in MR Images for Evaluation of Segmentation Efficacy. *Medical Image Analysis (MedIA)*, Vol 13, No 2, pp. 297-311, April 2009.

[26] Niethammer M, Hart G, Pace D, Vespa P, Irimia A, Van Horn J, Aylward S, Geometric Metamorphosis. Lecture Notes in Computer Science, Vol. 6893, *Medical Image Computing and Computer Assisted Intervention (MICCAI)*, pp. 639-646, 2011.

[27] Y. Zhuo, B. Sutton, X.-L. Wu, J. Haldar, W.-m. Hwu, Z.-P. Liang. Sparse Regularization in MRI Iterative Reconstruction Using GPUs. *Proc BMEI*, Yantai, pages 578-582, 2010.

[28] P. Thévenaz, M. Unser. Optimization of Mutual Information for Multiresolution Image Registration. *IEEE Transactions on Image Processing*, vol. 9, no. 12, pp. 2083-2099, December 2000.

[29] D. Loeckx, F. Maes, D. Vandermeulen, P. Suetens. Nonrigid image registration using free-form deformations with a local rigidity constraint. *Medical Image Computing and Computer-Assisted Intervention (MICCAI)*, pp. 639-646, 2004.

[30] G. Christensen and J. He. Consistent nonlinear elastic image registration. *In Proc. of MMBIA*, 2001.

[31] D. Rueckert, L. I. Sonoda, C. Hayes, D. L. G. Hill, M. O. Leach, and D. J. Hawkes, Non-rigid registration using free-form deformations: Application to breast MR images, *IEEE Trans. Med. Imag.*, vol. 18, pp.712-721, 1999.

[32] Clatz, O., Sermesant, M., Bondiau, P.-Y., Delingette, H., Warfield, S.K., Malandain, G., Ayache, N., Realistic simulation of the 3D growth of brain tumors in MR images including diffusion and mass effect. *IEEE Trans. Med. Imaging 24 (10)*, pp. 1344-1346, 2005.

[33] W. Shi , X. Zhuang , L. Pizarro , W. Bai , H. Wang , K.-P. Tung , P. Edwards and D. Rueckert. Registration using sparse free-form deformations. *Proc. Int. Conf. Med. Image Comput. Comput.-Assist. Intervent.*, pp.65-66, 2012.

Master thesis filing card

Student: Xavier Garcia Pich

Title: Exploiting Sparsity for Registration of Brain Tumor MR Images

UDC: 621.3

Abstract:

In medical imaging, sparsity has been used in the acquisition and reconstruction of MRI images, image denoising and face recognition among others. The aim of this thesis is to assess whether exploiting sparsity is a desirable property in the problem of brain tumor image registration. To this end, we consider tumor mass effect and tumor infiltration as two different tumor growing effects. In intensity-based nonrigid image registration, an optimization problem is defined by the minimization of a cost function with respect to the transformation parameters. This cost function consists of a dissimilarity term between the images being registered and a term that regularizes the transformation. Within this thesis, a modified ℓ_1 norm dissimilarity measure and a modified ℓ_1 regularization term are constructed. We compare the performance of different algorithms that combine these contributions with an ℓ_2 norm dissimilarity measure and diffusion regularizer for three different transformation models. Methods are tested on simulated brain tumor MR images and the validation of the registration is done by computing two dissimilarity distances between the deformation field obtained and a simulated ground truth. Results show that algorithms that use the modified ℓ_1 regularizer and a ℓ_2 dissimilarity measure recover the deformation of the tumor, while algorithms that use the modified ℓ_1 norm dissimilarity measure in some situations do not.

Thesis submitted for the degree of Telecommunications Engineering

Thesis supervisor: prof. dr. ir. Frederik Maes

Assessor:

Mentors: dr. Thijs Dhollander
ir. Tom Haeck